Energy budget-based backscatter in a non-linear shallow water model driven by double gyre wind forcing

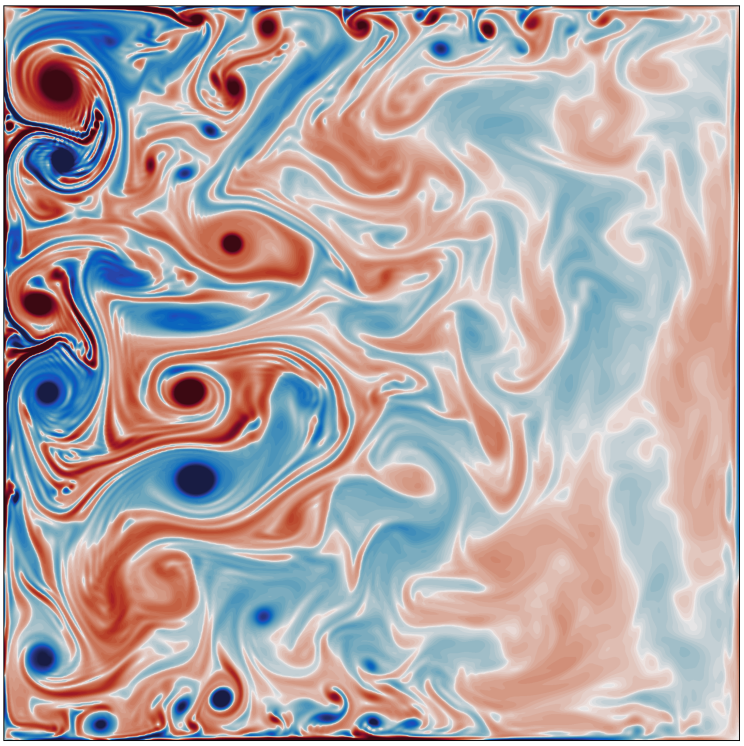

Milan Klöwer
GEOMAR Helmholtz Centre for Ocean Research Kiel
Christian-Albrechts-Universität zu Kiel

Advisor: Prof. Dr. Richard Greatbatch
Co-advisor: Dr. Sören Thomsen

A thesis submitted for the degree of
Master of Science
in the subject
Climate Physics: Meteorology and Physical Oceanography

Kiel, September 2017

Abstract

The parametrization of sub-grid scale processes is one of the key challenges towards improved numerical simulations of atmospheric and oceanic circulation. Numerical weather prediction models as well as climate models would benefit from more sophisticated turbulence closures that allow for less spurious dissipation at the grid-scale and consequently higher and more realistic levels of eddy kinetic energy (EKE). Recent studies [Jansen & Held, 2014; Jansen *et al.*, 2015] propose to use a hyperviscous closure in combination with an additional deterministic forcing term as a negative viscosity to represent backscatter of energy from unresolved scales. The sub-grid EKE is introduced as an additional prognostic variable [Eden & Greatbatch, 2008] that is fed by dissipation at the grid scale, and enables recycling of EKE via the backscatter term at larger scales. This parametrization was shown to work well in a primitive equation model in channel configuration. Here, we apply the parametrization to a shallow water model driven by double gyre wind forcing with no-slip boundary conditions and provide evidence for its general application. Introducing a Rossby number-based scaling for the strength of the backscatter, which is physically based on upscale (downscale) cascades of balanced (unbalanced) flow, we overcome essentially the numerical instabilities at the boundary that otherwise limit the practicability of the backscatter parametrization. In terms of mean state and variability, a coarse resolution model is largely improved towards a high resolution truth at low additional computational cost.

Zusammenfassung

Die Parametrisierung von Prozessen, die auf Skalen kleiner als der Gittergröße ablaufen, ist eine der wesentlichen Herausforderungen im Hinblick auf verbesserte numerische Simulationen von atmosphärischer und ozeanischer Zirkulation. Numerische Wettervorhersagemodelle wie auch Klimamodelle würden von anspruchsvolleren Turbulenzparametrisierungen, die eine geringere Dissipation auf der Gitterskala und dementsprechend höhere und realistischere Level von kinetischer Eddyenergie (EKE) erlauben, profitieren. Kürzlich publizierte Studien [Jansen & Held, 2014; Jansen *et al.*, 2015] schlagen vor, Hyperviskosität in Kombination mit einem zusätzlichen deterministischen Antriebsterm, welcher als negative Viskosität Rückstreuung von Energie der nicht aufgelösten Skalen repräsentiert, zu benutzen. Die EKE der sub-Gitterskala wird als eine zusätzliche prognostische Variable [Eden & Greatbatch, 2008] eingeführt, die von der Dissipation auf der Gitterskala versorgt wird und eine Zurückführung von EKE zu größeren Skalen mittels des Rückstreuterms erlaubt. Es wurde gezeigt, dass diese Parametrisierung mit den primitiven Gleichungen in Kanalkonfiguration gut funktioniert. Hier wenden wir diese Parametrisierung in einem Flachwassermodell mit no-slip Randbedingungen an, welches mit Wind angetrieben wird, der zwei große ozeanische Wirbel erzeugt, und liefern Belege für eine allgemeine Verwendbarkeit der Parametrisierung. Mit Hilfe einer Skalierung der Rückstreustärke basierend auf der Rossbyzahl, welche physikalisch auf Auf- und Abwärtskaskaden von un- und ausbalancierter Strömung beruhen, überwinden wir die numerischen Instabilitäten an den Rändern, die sonst die Verwendbarkeit der Rückstreuparametrisierung limitieren. Ein grob aufgelöstes Modell wird im Sinne von Klimatologie und Variabilität deutlich in Richtung eines hochaufgelösten Referenzmodells verbessert und das bei geringem zusätzlichen Rechenaufwand.

Contents

Chapter 1

Introduction

Mesoscale eddies are a key turbulent feature of the global oceans. Understanding their complex interplay with the large-scale circulation [Marshall, 1984; Wunsch & Ferrari, 2004] is a major challenge in climate research, inevitably important to assess and predict climate change [Flato *et al.*, 2013; Randall *et al.*, 2007; Vallis, 2016]. Eddies are capable of transferring energy across scales and are therefore a crucial element in the ocean's energy cycle [Aiki *et al.*, 2016], which's closure in ocean general circulation models is an active field of research [Eden, 2016]. Western boundary currents (e.g. Gulf Stream and Kuroshio) and their extension regions, being responsible for an essential part in the global meridional overturning circulation [Bigg *et al.*, 2003; Wunsch, 2002], as well as the Southern Ocean show an enhanced eddy activity ranging from several hundreds of kilometer down to the kilometer scale [Ferrari & Wunsch, 2010]. Hence, eddies are main drivers of tracer transport and dominate effectively the mixing and stirring of physical, chemical and biological water mass properties.

In the near future, state-of-the-art climate models will approach spatial resolutions at which the largest eddies can be resolved explicitly [Eyring *et al.*, 2016]. However, societally imporant climate predicitions of the next century still involve simplistic parametrizations of the full eddy spectrum and therefore largely contribute to the uncertainties of climate change projections. Despite the increasing performance of supercomputers, the most advanced Earth system models are not expected to fully resolve the mesoscale let alone the submesoscale [McWilliams, 2016] within the next decades. The need for more sophisticated turbulence closures, realistically parametrizing the effect

of meso- and submesoscale eddies on the resolved flow, is hence clear.

Traditional approaches to eddy parametrization are downgradient [Gent & McWilliams, 1990], ensuring numerical stability [Griffies, 2004], although evidence exists that eddies also affect the mean circulaton via upgradient momentum fluxes [Greatbatch *et al.*, 2010]. Many approaches neglect sub-grid scale variability and parametrizations are formulated as a function of the resolved flow, leading to a strong underestimation of the effective number of variables that determine the future evolution of the flow field [Palmer, 2001]. Physically motivated is the implementation of eddy viscosities or eddy diffusivities to mimic the general tendency of the eddy field to mix and hence smooth gradients. In that sense, there are two requirements to frictional operators in ocean circulation models: (i) the physical parametrization of friction, successive instabilities and thus mixing; and (ii) numerical stability, due to which viscosity coefficients are several orders of magnitude larger as would result from molecular considerations [Griffies & Hallberg, 2000]. We therefore believe successful parametrizations should aim to close the energy cycle by reducing the effective viscosity that otherwise leads to a spurious energy dissipation at the grid scale [Arbic *et al.*, 2007; Eden, 2016; Jansen & Held, 2014].

Eddy parametrizations that allow for upscale and downscale fluxes of energy are currently under investigation (e.g. Eden & Greatbatch [2008]; Porta Mana & Zanna [2014]; Zanna *et al.* [2017]). A recently proposed approach [Jansen & Held, 2014; Jansen *et al.*, 2015] involves the combination of a hyperviscous closure in order to remove energy and enstrophy from the grid scale with a prognostic variable for the sub-grid EKE. The dissipated eddy kinetic energy is conserved and progressively reinjected into the resolved flow at larger scales via a deterministic term that is formulated as negative Laplacian viscosity. The effectively reduced dissipation allows for higher levels of eddy kinetic energy yielding an optimizing effect on mean state and large-scale variability. The approach was tested in an idealized ocean model based on the primitive equations in channel configuration. Here, we apply the parametrization to a shallow water model driven by double gyre wind forcing with no-slip boundary conditions and provide evidence for its general application.

This thesis is structured as follows. Chapter 2 briefly presents the shallow water model used throughout this study and its energetics. The

formulation of sub-grid scale eddy kinetic energy and the resulting energy budget-based backscatter parametrization is introduced subsequently. In Chapter 3 we discuss the model bias of the low resolution control run without parametrization compared to the high resolution truth as reference. The impact of the energy budget-based backscatter parametrization on the low resolution model is analysed in Chapter 4. Finally, we summarize and discuss the results in Chapter 5. Appendices A.1-A.3 provide details about the discretization of the shallow water equations and derivations concerning the energy equation.

Chapter 2

Methodology

This chapter describes the methods that are used in this study. Prior to the methodology, the notation used in this chapter is explained in section 2.0. Section 2.1 introduces the shallow water model whose simulations are used throughout this study. Energetics in the shallow water model and the formulation of the backscatter parametrization are succeedingly discussed in section 2.1.4. The analysis of Reynolds and Rossby numbers is based on definitions provided in section 2.3. In section 2.4, details on the computation of the eddy kinetic energy spectrum are given. The analysis of Lagrangian trajectories is presented in section 2.5 and finally a short remark on the data sampling from the shallow water model is provided in section 2.6.

2.0 Notation

In the following, we will make use of a notation, where

(i) a scalar variable a, A is written in normal font with either lower or upper case letter. A vector $\mathbf{a} = (a_1, a_2)$ is written in bold-font but lower case. A tensor $\mathbf{A} = (A_1, A_2; A_3, A_4)$ is written with upper case bold letters.

(ii) the product $\cdot$ between a vector $\mathbf{a} = a_i$ and a tensor $\mathbf{C} = C_{ij}$ is defined as $\mathbf{a} \cdot \mathbf{C} = \sum_i a_i C_{ij} = d_j$ and yields a vector $d_j = \mathbf{d}$.

(iii) two vectors $\mathbf{a} = (a_1, a_2), \mathbf{b} = (b_1, b_2)$ concatenated without any symbol, i.e. $\mathbf{ab}$, yield a tensor $\mathbf{C}$, such that $\mathbf{ab} = (a_1 b_1, a_1 b_2; a_2 b_1, a_2 b_2) = \mathbf{C}$. Example given: $\nabla \mathbf{u} = (\partial_x u, \partial_x v; \partial_y u, \partial_y v)$

(iv) the 2-norm of a vector $\mathbf{a} = (a_1, a_2)$ is written as $|\mathbf{a}| = \sqrt{a_1^2 + a_2^2}$. Similarly the 2-norm of the tensor $\mathbf{A}$ is $|\mathbf{A}| = \sqrt{A_1^2 + A_2^2 + A_3^2 + A_4^2}$. For a complex number $z = a + ib$, $|z| = \sqrt{a^2 + b^2}$.

2.1 The shallow water model

The shallow water model follows from the depth-integrated Navier-Stokes equations with the assumption that the vertical length scale is negligible compared to the horizontal length scale [Gill, 1982; Vallis, 2006]. In this study we use the shallow water equations of the form

$$\partial_t u + u\partial_x u + v\partial_y u - fv = -g\partial_x \eta + F_x + B_x + M_x + \xi_x \tag{2.1a}$$

$$\partial_t v + u\partial_x v + v\partial_y v + fu = -g\partial_y \eta + F_y + B_y + M_y + \xi_y \tag{2.1b}$$

$$\partial_t \eta + \partial_x(uh) + \partial_y(vh) = 0 \tag{2.1c}$$

with

$\mathbf{u} = (u, v) = (u(x, y, t), v(x, y, t))$	horizontal velocity vector
$\eta = \eta(x, y, t)$	surface displacement
$h = h(x, y, t) = \eta + H$	layer thickness
$H =$ constant	undisturbed layer thickness
$f = f(y)$	Coriolis parameter
$g =$ constant	gravitational acceleration
$\mathbf{f} = (F_x, F_y) = (F_x(x, y, t), F_y(x, y, t))$	forcing vector
$\mathbf{b} = (B_x, B_y) = (B_x(u, v, h), B_y(u, v, h))$	bottom friction term
$\mathbf{m} = (M_x, M_y) = (M_x(u, v, h), M_y(u, v, h))$	lateral mixing of momentum
$\mathbf{\Xi} = (\xi_x, \xi_y)$	negative viscosity backscatter

and differential operators $\partial_x = \frac{\partial}{\partial x}, \partial_y = \frac{\partial}{\partial y}, \partial_t = \frac{\partial}{\partial t}$ on the rectangular domain $\mathcal{D} = (0, L_x) \times (0, L_y)$ of width (or east-west extent) L_x and north-south extent L_y and with cartesian coordinates x, y and time t. As initial conditions we choose to start from rest, so that $u = v = \eta = 0$ at $t = 0$. There is no flow through the boundary, which is usually referred to as the kinematic boundary condition (equaton A.1). We set the tangential velocity at the boundary to zero in order to have no-slip boundary conditions (equation A.3). This is motivated as free-slip boundary conditions (equation A.4) in contrast yield an enormous western boundary current that is maintained by eddies propagating via the northern boundary towards the east. In order to

have some resemblance of the shallow water model with the circulation in mid-latitudinal ocean basins, we favour no-slip boundary conditions.

In the following, the formulation of the terms appearing in the shallow water equations 2.1 are presented. A detailed description about the discretization of the shallow water equations 2.1 is found in appendix A.2. It is based on an equivalent formulation of the shallow water equations as presented in appendix A.1.2.

2.1.1 Barotropic double gyre wind forcing

In order to simulate mid-latitudinal dynamics, we choose the physical parameters of the previous section as [Berloff, 2005; Cooper & Zanna, 2015; Porta Mana & Zanna, 2014; Zanna *et al.*, 2017]

$$g = 10 \text{ ms}^{-2}, \quad H = 500 \text{ m}, \quad L_x = L_y = 3840 \text{ km} \tag{2.2}$$

with beta-plane approximation [Gill, 1982]

$$f = f_0 + \beta(y - \frac{L_y}{2}), \quad f_0 = 2\Omega \sin(2\pi \frac{\theta_0}{360}), \quad \beta = \frac{2\Omega}{R} \cos(2\pi \frac{\theta_0}{360}) \tag{2.3}$$

at northern hemisphere mid-latitudes, with the domain $\mathcal{D}$ being centred around the latitude $\theta_0 = 30$ with

$$R = 6371 \text{ km}, \quad \Omega = \frac{2\pi}{86400} \text{ s}^{-1}. \tag{2.4}$$

The forcing is set to be $F_y = 0$ and

$$F_x = \frac{\gamma}{\rho h} \tag{2.5a}$$

$$\gamma = F_0 \left[\cos\left(2\pi \left(\frac{y}{L_y} - \frac{1}{2}\right)\right) + 2 \sin\left(2\pi \left(\frac{y}{L_y} - \frac{1}{2}\right)\right)\right] \tag{2.5b}$$

with amplitude $F_0 = 0.12$ Pa and density $\rho = 1000$ kgm^{-3}. The forcing F_x resembles the trade winds in the southern part of the domain and the westerlies in the northern part of the domain (Fig. 2.1). We admit that the choice of H yields an unrealistically shallow ocean basin. The wind forcing is increased by a factor of three compared to reference values [Cooper & Zanna, 2015]. However, we thereby increase the allowed numerical time step (see section A.2.9) leading to a reduced effective computing time for a more

turbulent shallow water system.

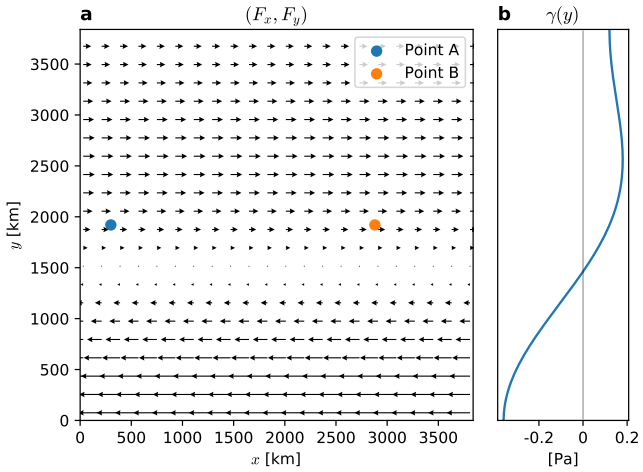

Figure 2.1: (a) The wind forcing (F_x, F_y) resembling trade winds and westerlies over the domain $\mathcal{D}$. (b) Wind profile γ. The points A, B will used for the analysis of autocorrelation (section 3.6, Fig. 3.10 and 3.11).

2.1.2 Bottom friction

A quadratic drag of the following form is used for all model runs with bottom friction

$$\mathbf{b} = -\frac{c_D}{h}|\mathbf{u}|\mathbf{u} \tag{2.6}$$

with c_D being a dimensionless drag coefficient [Arbic & Scott, 2008]. In contrast to a linear drag, a quadratic drag was found to be more realistic. It removes energy especially at the larger scales, leaving the smaller scales almost unaffacted. This is supported in this study (see section 3.4).

The energetics of the bottom friction term are presented in section 2.1.4. In this study, we investigate a set of model runs containing bottom friction where we choose $c_D = 10^{-5}$ and another set of model runs without bottom friction ($c_D = 0$) as described in Table 2.1. The choice of c_D is discussed in section A.2.6.

2.1.3 Lateral mixing of momentum

The viscosity is formulated as lateral mixing of momentum and represented by the term $\mathbf{m}$. A general approach $\mathbf{m}_0$ of this family being

$$\mathbf{m}_0 = \nabla \cdot \nu \mathbf{S} \tag{2.7}$$

with the viscosity coefficient ν and a stress tensor $\mathbf{S}$ (sometimes also called viscous flux tensor [Eden, 2016]). With $\mathbf{S} = \nabla \mathbf{u}$ and a constant ν the equation 2.7 reduces to

$$\mathbf{m}_L = \nu \nabla^2 \mathbf{u} \tag{2.8}$$

with $\nabla^2 = \partial_x^2 + \partial_y^2$ the two dimensional Laplace operator. However, as discussed by Shchepetkin & O'Brien [1996] a more sophisticated alternative is found with the symmetric 2x2 stress tensor $\mathbf{S}$ defined by

$$\mathbf{S} = \begin{pmatrix} u_x - v_y & v_x + u_y \\ v_x + u_y & -(u_x - v_y) \end{pmatrix}. \tag{2.9}$$

Their harmonic lateral mixing of momentum term $\mathbf{m}_2$ is then formulated for the shallow water model as

$$\mathbf{m}_2 = \nu_A h^{-1} \nabla \cdot h\mathbf{S}. \tag{2.10}$$

Note that for h being a constant equation 2.10 simplifies to equation 2.8. Equation 2.10 can be extended to a biharmonic operator by applying it twice

$$\mathbf{m} = \nu_B h^{-1} \nabla \cdot (h\mathbf{S}(h^{-1} \nabla \cdot h\mathbf{S}(u, v))). \tag{2.11}$$

where the stress tensor is regarded as a linear map, once evaluated with (u, v) and then with $h^{-1} \nabla \cdot h\mathbf{S}(u, v)$. Both viscosity coefficients ν_A and ν_B are for simplicity taken as constants. Again, for a constant h equation 2.11 reduces to $\nu_B \nabla^4 \mathbf{u}$, with $\nabla^4 = \partial_x^4 + \partial_y^4 + 2\partial_x^2 \partial_y^2$. Hence, for a barotropic system, where $\eta \ll H$ it might be justified to linearize the viscous term by assuming h to be constant as in Cooper & Zanna [2015]. However, here we keep the form of equation 2.11 to have a fully non-linear system. A higher order derivative implies the use of higher order boundary conditions: Applying the harmonic

operator twice yields additional boundary conditions as

$$h\nabla^2 u + \nabla h \cdot \begin{pmatrix} u_x - v_y \\ v_x + u_y \end{pmatrix} = 0, \quad \text{at} \quad x = 0 \quad \text{and} \quad x = L_x \tag{2.12}$$

and

$$h\nabla^2 v + \nabla h \cdot \begin{pmatrix} v_x + u_y \\ v_y - u_x \end{pmatrix} = 0, \quad \text{at} \quad y = 0 \quad \text{and} \quad y = L_y \tag{2.13}$$

For the case of a constant h this simplifies to a vanishing second derivative of the normal velocity component at the boundaries.

A biharmonic operator acts especially on the small scales, where waves are rapidly damped compared to the large scales, which remain mostly unaffected [Griffies & Hallberg, 2000; Shchepetkin & O'Brien, 1996]. To have an additional energy sink at the large scales, bottom friction from equation 2.6 is used in combination with the biharmonic lateral mixing of momentum as presented here. For a discussion on the choice of ν_B the reader is referred to section A.2.6. The choices for the different model runs are listed in Table 2.1.

2.1.4 Energetics in the shallow water model

In the following, energy sources/sinks and reservoirs in the shallow water system are discussed as they will be analyzed for all model runs in section 3.4.

The shallow water equations without forcing or dissipation (i.e. $\mathbf{f} = \mathbf{m} = \mathbf{b} = 0$) obey a conservation of energy of the form

$$\partial_t \langle \tfrac{1}{2}\rho h(u^2 + v^2) + \tfrac{1}{2} g\rho\eta^2 \rangle = 0. \tag{2.14}$$

For a detailed derivation see Appendix A.3.1. The first term represents kinetic energy KE and the second (available) potential energy PE, both horizontally integrated by $\langle\rangle = \iint_{\mathcal{D}} \mathrm{d}\mathbf{x}$ and vertically as are the momentum equations (2.1).

Energetics of wind forcing Once we consider wind forcing F_x in equation 2.1a of the form as in equation 2.5

$$\partial_t u = ... + \frac{\gamma}{\rho h} \tag{2.15}$$

the energy $\langle \mathrm{KE} + \mathrm{PE} \rangle$ is not conserved

$$\partial_t \langle \mathrm{KE} + \mathrm{PE} \rangle = \langle u\gamma \rangle \tag{2.16}$$

Once u and F_x are of the same sign, i.e. the flow follows the direction of the wind, the wind forcing term is a source of energy to the shallow water system. As we start the model runs from rest we can expect at least in the sense of a spatial and temporal average that the wind forcing is a source of energy to the shallow water system. This is discussed and supported in section 3.4.

Energetics of bottom friction Consider adding a drag term of the form in equation 2.6

$$\partial_t \mathbf{u} = ... - \frac{c_D}{h}\sqrt{u^2 + v^2}\mathbf{u} \tag{2.17}$$

that acts physically as bottom friction. The energy equation is then

$$\partial_t \langle \mathrm{KE} + \mathrm{PE} \rangle = -\langle \rho c_D (u^2 + v^2)^{\frac{3}{2}} \rangle \leq 0. \tag{2.18}$$

which is with non-vanishing velocities an energy sink throughout the domain $\mathcal{D}$ at every time step.

Energetics of lateral mixing A term of the form

$$\partial_t \mathbf{u} = ... + h^{-1}\nabla \cdot (\nu h \mathbf{S}) \tag{2.19}$$

with viscosity coefficient $\nu > 0$ and stress tensor $\mathbf{S}$ is added to the momentum equations. In fact, using a biharmonic lateral mixing of momentum this term should be negative to account for the correct sign of diffusion. Adaptation of the following for a biharmonic operator is straight forward. The energy equation is then

$$\partial_t \langle \mathrm{KE} + \mathrm{PE} \rangle = \langle \rho \mathbf{u} \cdot (\nabla \cdot \nu h \mathbf{S}) \rangle. \tag{2.20}$$

By evaluating

$$\mathbf{u} \cdot (\nabla \cdot \nu h \mathbf{S}) = \nabla \cdot (\nu h \mathbf{S} \cdot \mathbf{u}) - \nabla \mathbf{u} \cdot \nu h \mathbf{S} \tag{2.21}$$

and making use of the kinematic boundary condition the first term vanishes in the global integral as divergence of a flux and it follows that

$$\partial_t \langle \mathrm{KE} + \mathrm{PE} \rangle = -\langle \rho \nu h \nabla \mathbf{u} \cdot \mathbf{S} \rangle. \tag{2.22}$$

For the case of $\mathbf{S}$ being the symmetric stress tensor defined in equation 2.9, i.e. harmonic diffusion, lateral mixing is an energy sink as $\partial_t \langle \mathrm{KE} + \mathrm{PE} \rangle = -\langle \rho \nu h \nabla \mathbf{u} \cdot \mathbf{S} \rangle \leq 0$ not just spatially integrated but everywhere in the domain $\mathcal{D}$ (see section A.3.3 for details). This is in contrast to biharmonic mixing operators (equation 2.11), which are not sign-definite in that respect. As a result, the harmonic diffusion is always down-gradient, but the biharmonic diffusion can also lead to local power input in equation 2.22 [Griffies, 2004], but is in general also an energy sink.

Mean and eddy kinetic and potential energy Using Reynolds - decomposition in time allows to split every quanitity a into a time mean $\overline{a}$ and anomalies a' relative to $\overline{a}$ as

$$a = \overline{a} + a'. \tag{2.23}$$

However, in the shallow water system it is proposed to use thickness-weighted averaging [Aiki *et al.*, 2016]

$$\widehat{a} = \frac{\overline{ha}}{\overline{h}} \tag{2.24}$$

The thickness-weighted average $\widehat{a}$ is then used to compute the respective anomalies a''

$$a'' = a - \widehat{a} \tag{2.25}$$

Note that $\overline{ha''} = 0$. We can split the potential energy PE into mean potential energy (MPE) and eddy potential energy (EPE) with the thickness-unweighted decomposition

$$\overline{\mathrm{PE}} = \overline{\tfrac{1}{2} g \rho (\overline{\eta} + \eta')^2} = \tfrac{1}{2} g \rho \overline{\eta}^2 + \tfrac{1}{2} g \rho \overline{\eta'^2} \equiv \mathrm{MPE} + \mathrm{EPE}\,. \tag{2.26}$$

For mean kinetic energy (MKE) and eddy kinetic energy (EKE) we use thickness-weighted decomposition on u and v

$$\begin{aligned}\overline{\mathrm{KE}} &= \overline{\tfrac{1}{2}\rho h\left((\widehat{u}+u'')^2+(\widehat{v}+v'')^2\right)}\\ &= \tfrac{1}{2}\rho\left(\overline{h(\widehat{u}^2+\widehat{v}^2)+h(u''^2+v''^2)+2\widehat{u}hu''+2\widehat{v}hv''}\right)\\ &= \tfrac{1}{2}\rho\overline{h}(\widehat{u}^2+\widehat{v}^2)+\tfrac{1}{2}\rho\overline{h(u''^2+v''^2)}\\ &\equiv \mathrm{MKE}+\mathrm{EKE}\end{aligned} \tag{2.27}$$

2.2 Formulation of the energy budget-based backscatter parametrization

Following the ideas of Eden & Greatbatch [2008] for a mesoscale eddy closure, which are further developed in Jansen & Held [2014]; Jansen *et al.* [2015] we seek to find an energy equation for the unresolved scales, i.e. an equation for the sub-grid eddy kinetic energy e, applied to the shallow water equations. Similar to Jansen *et al.* [2015] we formulate

$$\partial_t e = -\dot{E}_{\mathrm{diss}} + \dot{E}_{\mathrm{back}} + \nabla\cdot\nu_e\nabla e \tag{2.28}$$

with $\dot{E}_{\mathrm{diss}}$ being the tendency representing the dissipation of the resolved flow that results from biharmonic viscosity. Adding this term to the prognostic equation of sub-grid EKE e is therefore a transfer of energy from the resolved to the unresolved flow. The term $\dot{E}_{\mathrm{back}}$ represents the tendency associated with the backscatter parametrization. It is the effect of energy transfer from the sub-grid EKE budget back onto the resolved flow and is realized with negative Laplacian viscosity. The last term of the right-hand side is a diffusion of sub-grid EKE.

For the shallow water model (equations 2.1) the local dissipation of eddy kinetic energy $\dot{E}_{\mathrm{diss}}$ associated with biharmonic viscosity (equation 2.11) is in close relation to the energy equation 2.22. Omitting the constant density ρ and the flux terms appearing in equations 2.21 and A.83 yields

$$\dot{E}_{\mathrm{diss}} = c_{\mathrm{diss}}\nu_B h\nabla\mathbf{u}\cdot\mathbf{S}^* \tag{2.29}$$

with the biharmonic stress tensor $\mathbf{S}^* = \mathbf{S}(h^{-1}\nabla\cdot h\mathbf{S}(u,v)))$ based on the symmetric stress tensor $\mathbf{S}$ from equation 2.9. $\dot{E}_{\mathrm{diss}}$ is negative where the

biharmonic lateral mixing of momentum removes energy from the resolved flow, which is usually the case. In contrast to Jansen *et al.* [2015] we introduce a spatially and time-varying scaling c_{diss} which obeys

$$0 \leq c_{\text{diss}}(\mathbf{x}, t) \leq 1 \tag{2.30}$$

to allow only a fraction of the dissipated EKE to enter the sub-grid EKE budget. This is done for the following reasons:

(i) Having $c_{\text{diss}} \leq 1$ yields an additional energy sink for the resolved flow, as the fraction $1 - c_{\text{diss}}$ is eventually dissipated and not subject to the recycling process of the backscatter parametrization. This might be as well desired for reasons of numerical stability. In case of vanishing bottom friction ($\mathbf{b} = 0$), chosing $c_{\text{diss}} = 1$ would easily lead to an effective dissipation (taking both, biharmonic viscosity and the negative viscosity effect from backscatter, into account) that is too weak and below the allowed range to remain numerically stable.

(ii) In general, we can expect some flow dependence on the direction of energy cascades (upscale or downscale), which allows dissipation conditioned on properties of the locally resolved flow.

In order to match these, it is proposed to use

$$c_{\text{diss}} = \frac{1}{(1 + R_o^*)^{n_{\text{diss}}}} \tag{2.31}$$

with the deformation rate-based Rossby number R_o^* (see equation 2.43), which is per definition non-negative. Hence, equation (2.31) obeys the condition of equation (2.30) for a positive constant n_{diss} which remains subject to tuning. Having a deformation rate-based scaling of dissipation via c_{diss} comes with the advantage that regions of strong shear, especially boundary currents that are subject to no-slip boundary conditions, experience a stronger dissipation than elsewhere. This avoids reinjecting an excess amount of energy via the backscatter terms locally where it may lead to spurious oscillations at the grid scale, that eventually lead to numerical instabilities. Physically speaking, we want to overcome the spurious energy dissipation at the grid scale for balanced flows, which tend to have a small Rossby number (which leads to c_{diss} being close to 1) but retain the dissipative character for unbalanced flows

with large Rossby number [Rhines, 1979; Zhai *et al.*, 2010]. This is motivated as geostrophic turbulence at small Rossby numbers tends to undergo an upscale cascade of energy, whereas large Rossby numbers are indicative of a downscale cascade where energy should indeed be dissipated [Brüggemann & Eden, 2015; Ferrari & Wunsch, 2009; Molemaker *et al.*, 2010].

Once the backscatter is realized with a negative Laplacian viscosity, that means the backscatter forcing terms in the shallow water equations (2.1) take the form

$$(\xi_x, \xi_y) = h^{-1}\nabla \cdot \nu_{\text{back}} h\mathbf{S} \tag{2.32}$$

with a negative viscosity coefficient ν_{back} that is defined in equation 2.34. It follows that

$$\dot{E}_{\text{back}} = \nu_{\text{back}} h\nabla\mathbf{u} \cdot \mathbf{S} \tag{2.33}$$

In contrast to Jansen *et al.* [2015], using a shallow water model, we consider the vertically integrated sub-grid EKE e of units m^3s^{-2}, which alters the scaling for ν_{back} slightly through dividing by h

$$\nu_{\text{back}} = -c_{\text{back}}\Delta x\sqrt{\max(2\frac{e}{h}, 0)} \tag{2.34}$$

so that ν_{back} retains its physical units as m^2s^{-1}. c_{back} is an order $\mathcal{O}(1)$ non-dimensional constant, which we set as proposed in Jansen *et al.* [2015] to be 0.4 and do not perform sensitivity experiments as general dependence was shown to be weak. Equation 2.28 can predict negative values of e, hence using the maximum guarantees no backscatter in this case.

To summarize, we extend the shallow water equations with a prognostic equation for the vertically-integrated sub-grid EKE e that is

$$\partial_t e = -c_{\text{diss}}\nu_B h\nabla\mathbf{u} \cdot \mathbf{S}^* + \nu_{\text{back}} h\nabla\mathbf{u} \cdot \mathbf{S} + \nabla \cdot \nu_e \nabla e. \tag{2.35}$$

From the perspective of the sub-grid EKE, the first term acts as a forcing, the second is a damping term as ν_{back} is non-positive, $h\nabla\mathbf{u} \cdot \mathbf{S} \geq 0$ (see A.3.3) and monotonically decreasing with e; and the third is a diffusion term, and we set $\nu_e = \nu_A$ (see section A.2.6).

Computational aspects For completeness, it is pointed out that the following simplifications for equations 2.29 and 2.33 hold:

$$\dot{E}_{\text{diss}} = c_{\text{diss}} \nu_B h \left(\mathbf{S}_{11} \mathbf{S}_{11}^* + \mathbf{S}_{12} \mathbf{S}_{12}^* \right), \quad \dot{E}_{\text{back}} = \nu_{\text{back}} h \left(\mathbf{S}_{11}^2 + \mathbf{S}_{12}^2 \right) \tag{2.36}$$

with a derivation in appendix A.3.2.

2.3 Reynolds and Rossby numbers

Definitons of the Reynolds and Rossby numbers directly calculated from the size of terms in the shallow water equations and adapted to the energy budget-based backscatter parametrization are presented.

Reynolds number The Reynolds number, defined as the ratio between advective and viscous terms, is traditionally estimated via scale analysis

$$\widehat{R_e} = \frac{\mathcal{O}((\mathbf{u} \cdot \nabla)\mathbf{u})}{\mathcal{O}(\nu \nabla^2 \mathbf{u})} = \frac{UL}{\nu} \tag{2.37}$$

with some velocity scale U, length scale L and viscosity ν. It is also possible to directly compute the size of the advective and viscous term, i.e. replacing the $\mathcal{O}()$-operation by the 2-norm of a vector and using the lateral mixing of momentum from equation (2.11)

$$R_e = \frac{|(\mathbf{u} \cdot \nabla)\mathbf{u}|}{|\nu_B h^{-1} \nabla \cdot (h \mathbf{S}(h^{-1} \nabla \cdot h \mathbf{S}(u, v)))|} \tag{2.38}$$

In the case of the backscatter parametrization, the effective Reynolds number R_e^* also includes the backscatter term

$$R_e^* = \frac{|(\mathbf{u} \cdot \nabla)\mathbf{u}|}{|\nu_B h^{-1} \nabla \cdot (h \mathbf{S}(h^{-1} \nabla \cdot h \mathbf{S}(u, v))) + \nu_{\text{back}} h^{-1} \nabla \cdot h \mathbf{S}|} \tag{2.39}$$

in order to account for the negative viscosity introduced by the backscatter parametrization. In fact, the terms in the denominator counteract each other: The first tends to smooth gradients, whereas the second tends to steepen them. Using the backscatter parametrization we can expect that $R_e^* > R_e$ in an average sense.

Rossby number Via scale analysis the Rossby number $\widehat{R_o}$ results from the ratio of advective terms and Coriolis terms as

$$\widehat{R_o} = \frac{\mathcal{O}((\mathbf{u}\cdot\nabla)\mathbf{u})}{\mathcal{O}(f\mathbf{k}\times\mathbf{u})} = \frac{U}{fL} \tag{2.40}$$

with f being the Coriolis parameter and $\mathbf{k}$ the unity vector in the vertical. As in equation (2.38) the direct calculation for the Rossby number R_o yields

$$R_o = \frac{|(\mathbf{u}\cdot\nabla)\mathbf{u}|}{|f\mathbf{k}\times\mathbf{u}|}. \tag{2.41}$$

It is also possible to base an estimation R_o^* of the Rossby number on the deformation rate

$$|D| = \sqrt{(\partial_x u - \partial_y v)^2 + (\partial_y u + \partial_x v)^2} \tag{2.42}$$

which yields a large Rossby number R_o^* in regions with strong shear flow

$$R_o^* = \frac{|D|}{f} \tag{2.43}$$

Histogram computation The direct Reynolds numbers R_e and Rossby numbers R_o will be investigated in terms of their histogram computed for all grid cells and all available time steps (without the spin-up phase, see section 2.6) at daily resolution. Hence, the histograms are computed from roughly $1.5\cdot 10^8$ values in the low resolution case and $2.4\cdot 10^9$ at high resolution. The high resolution histograms are divided by a factor 16 to account for this and allow normalization onto the low resolution histograms. As Rossby and Reynolds numbers are approximately log-normally distributed the histogram is computed over their respective logarithms with a bin width of about 0.027 for Reynolds numbers and 0.018 for Rossby numbers. Also, a spatio-temporal mean Rossby and Reynolds number is computed, where the logarithm is applied afterwards for visualization purposes. For the model runs including backscatter, the effective Reynolds number R_e^* is used instead to account for the backscatter term.

Rossby radius of deformation The Rossby radius of deformation L_{R_o} is defined via the shallow water phase speed for gravity waves $c_{ph} = \sqrt{gH}$ (see discussion around equation A.75 for further details) and the Coriolis

parameter $f = f(y)$ as

$$L_{R_o} = \frac{c_{ph}}{f}. \tag{2.44}$$

In the beta-plane approximation (equation 2.3), the Rossby radius is largest at the southern edge of the domain ($y = 0$) and smallest at the northern edge ($y = L_y$), it is therefore further distinguished between

$$L_{R_o}^{\max} = \frac{c_{ph}}{f_0 - \beta\frac{L_y}{2}} \quad \text{and} \quad L_{R_o}^{\min} = \frac{c_{ph}}{f_0 + \beta\frac{L_y}{2}}. \tag{2.45}$$

2.4 Eddy kinetic energy spectrum

To have an objective analysis about the effect of sub-grid scale parametrizations, the eddy kinetic energy spectrum EKE(K) as a function of the total wavenumber $K = \sqrt{k^2 + l^2}$ is regarded. k is the zonal wavenumber (in x-direction), l the meridional wavenumber (in y-direction). Such a spectrum is especially sensitive to oscillations that may appear at the grid scale once dissipation is too weak. In this case, kinetic energy tends to pile up at the largest wave numbers, which results from the numerics and is physically undesired. The spectrum is defined as [Jansen *et al.*, 2015]

$$\mathrm{EKE}(K) = \frac{d}{dK} \iint\limits_{k^2+l^2<K^2} \frac{1}{2}\left(\overline{|\widehat{u}_t|^2} + \overline{|\widehat{v}_t|^2}\right) dkdl \tag{2.46}$$

with $\widehat{u}_t, \widehat{v}_t$ being the spectral transforms of the two dimensional fields u, v for a given time t. The overbar denotes a temporal mean. The EKE spectrum regarded here therefore describes the energy per wavenumber (regardless of the direction) averaged in spectral space over all available time steps.

2.5 Lagrangian trajectories

To calculate the trajectory of a Lagrangian float, we follow the idea that at a given time t the position $\mathbf{x}_p = (x_p, y_p)$ of that particle changes by passive advection of the flow field

$$\frac{dx_p}{dt} = u(\mathbf{x} = \mathbf{x}_p), \qquad \frac{dy_p}{dt} = v(\mathbf{x} = \mathbf{x}_p). \tag{2.47}$$

Providing the initial position of the float $\mathbf{x}_p(t=0)$ we can solve equation 2.47 numerically with a given flow field (u, v). As the flow field is gridded on the native model grid, which in general does not correspond to the float positions, we interpolate bilinearly from the four surrounding grid points. Taking the boundary conditions of the flow field into account, no float was observed to leave the domain $\mathcal{D}$. However, due to a vanishing flow some floats remain at the boundary for a long time, which is thought of to be physically reasonable.

Discretizing the time derivative in equation 2.47 is done with a predictor-corrector method (also known as trapezoidal rule, [Butcher, 2008]). With x_0, y_0 the intial positions at time $t = t_0$ and x_1, y_1 the positions at time $t = t_0 + \delta t$ this is

$$x_1 = x_0 + \frac{\delta t}{2}(u_0 + u_1), \quad y_1 = y_0 + \frac{\delta t}{2}(v_0 + v_1) \tag{2.48}$$

where $u_0 = u(t = t_0, \mathbf{x} = \mathbf{x}_0)$ and $v_0 = v(t = t_0, \mathbf{x} = \mathbf{x}_0)$ and $u_1 = u(t = t_0 + \delta t, \mathbf{x} = \mathbf{x}_1^*)$ and $v_1 = v(t = t_0 + \delta t, \mathbf{x} = \mathbf{x}_1^*)$ with the initial guess positions

$$x_1^* = x_0 + \delta t u_0, \qquad y_1^* = y_0 + \delta t v_0 \tag{2.49}$$

that are computed with Euler forward. The float trajectories are calculated offline, hence the time step δt is 6 hours, as this is the smallest time step at which data from the numerical model is stored. We calculate trajectories from a total 100,000 floats, that where injected at 1000 random starting dates (after the spin-up phase) in groups of 100 floats. The trajectories are then calculated forward in time for one year. The results are presented in terms of *accumulated float density*, which accounts for all floats that have been at the respective location at some time within one year after release. That means, accumulated float density is a histogram that counts all floats that have been in a given grid box (equal boxes of $\Delta x = \Delta y = 15$km are used), regardless of when they have been there within one year after release. The zero-isoline of that histogram therefore denotes the line that no float was able to cross within one year. As release locations, we pick for every float a random position within a rectangle that spans from $x = 100$km to $x = 200$km and from $y = 100$km to $y = 1920$km as marked in Fig. 3.12 to place the floats close to the boundary within the subtropical gyre (a discussion is given in section 3.7). If all floats were always far away from the boundary, then the

accumulated float density would be calculated from in total 146,000,000 float positions (100,000 floats at 1460 time steps that result from 6-hourly data for 365 days). However, as some floats stay for a long time close to the boundary, as discussed above, these are neglected from analysis by disregarding all float positions that are closer than 30km to the boundary. In practice, this means that 98% of all theoretical positions enter the analysis for the control runs and 94% for the model runs with backscatter.

2.6 Model runs and data sampling

For the list of model runs that are analysed in this study see Table 2.1.

List of model runs	c_D	N_x	Δx [km]	ν_B [$m^4 s^{-1}$]	n_{diss}	t_c
with bottom friction						
Low resolution (LR)	10^{-5}	128^2	30	$4.86 \cdot 10^{11}$	-	1
High resolution (HR)	10^{-5}	512^2	7.5	$7.59 \cdot 10^{9}$	-	50.2
LR + weak backscatter	10^{-5}	128^2	30	$4.86 \cdot 10^{11}$	$\frac{1}{2}$	1.39
LR + moderate backscatter	10^{-5}	128^2	30	$4.86 \cdot 10^{11}$	$\frac{1}{6}$	1.39
LR + strong backscatter	10^{-5}	128^2	30	$4.86 \cdot 10^{11}$	0	1.39
without bottom friction						
Low resolution (LR)	0	128^2	30	$4.86 \cdot 10^{11}$	-	0.93
High resolution (HR)	0	512^2	7.5	$7.59 \cdot 10^{9}$	-	46.7
LR + weak backscatter	0	128^2	30	$4.86 \cdot 10^{11}$	$\frac{1}{2}$	1.30
LR + moderate backscatter	0	128^2	30	$4.86 \cdot 10^{11}$	$\frac{1}{3}$	1.30
LR + strong backscatter	0	128^2	30	$4.86 \cdot 10^{11}$	$\frac{1}{4}$	1.30

Table 2.1: List of model runs used in this study. The choice of the bottom friction coefficient c_D and the biharmonic viscosity ν_B is discussed in section A.2.6. The tuning parameter for backscatter n_{diss} appears in equation 2.31. The total number of grid cells is denoted with N_x, the grid spacing with Δx. The computing time t_c is given in relation to the computing time of the low resolution control run with bottom friction. Please note that the computing time is only roughly estimated and strongly dependent on the computing architecture.

For the analyses in this study, we use from every model run daily in-

stantaneous values on the native model grid of 30 year long integrations. Spatial interpolation is only used in the computation of terms that involve prognostic variables from different grids (see section A.2.1). Only for the analysis of autocorrelation (section 3.6) and Lagrangian trajectories (section 3.7) 6-hourly data is used for a better temporal resolution. A spin-up phase of 5 years, as discussed in section 3.2, is disregarded from all analysis except the timeseries in Fig. 3.2.

Chapter 3

Model bias compared to the high resolution truth

This chapter presents a comparison of the two control runs that differ only by their spatial resolution and the viscosity coefficient that is altered accordingly. The control runs do not include the backscatter parametrization, which will be introduced in chapter 4.

As we investigate the backscatter parametrization in an idealized ocean model set-up, there are no observations for reference. Hence, we regard the high resolution runs as the best approximation of the truth that is available, or shortly the *truth*. In contrast, the low resolution run is regarded as the *model*, which claims to represent an ocean circulation with the same statistics as the high resolution truth. We therefore ignore implicitly, that also the high resolution truth is only an approximation towards a simulation with further increased resolution. From this perspective, this study only addresses the issue of a limited horizontal resolution in the range from eddy-permitting to eddy-resolving, which is however apparent in a wide range of ocean or climate models currently in use to simulate and understand the global climate system. Furthermore, based on the scale-invariance of the Navier-Stokes equations [Palmer, 2012] we expect this issue also to project similiarly onto smaller scales and hence also to be of great importance in numerical weather prediction [Shutts, 2015]. Obviously, we cannot expect the low resolution model to simulate eddies that are barely resolved in the high resolution truth nor can we expect larger eddies to occur synchronously in both control runs. However, we can demand the low resolution model to simulate statistically

the same ocean circulation in terms of mean state, energy, variability and a variety of other quantities. Section 3.3 describes the model bias in terms of the climatological mean state. It follows a discussion of how the model differs with respect to energy compared to the truth in section 3.4. How much the physical regime, measured with Rossby and Reynolds numbers, disagrees between model and truth is presented in section 3.5. Section 3.6 discusses model biases concerning time scales of the prognostic variables and is succeeded by an analysis of Lagrangian floats, how they spread differently in model and truth in section 3.7. A summary of model biases is given in section 3.8.

3.1 First view on the flow structure

Regarding snapshots of relative vorticity $\zeta = \partial_x v - \partial_y u$ and corresponding flow speeds $|\mathbf{u}| = \sqrt{u^2 + v^2}$ provides some insight into the dynamics simulated by both low resolution model and high resolution truth (Fig. 3.1). At high resolution, eddies of different sizes are apparent in most of the western part of the domain and especially also in the proximity of the southern and northern boundary (Fig. 3.1c). At low resolution, larger eddies are also simulated where the boundary current leaves the western boundary but they do not propagate as far into the domain (Fig. 3.1a). Also, the proximity of the northern and the southern boundary are rather eddy-free. The circulation dynamics are mostly dominated by westwards propagating Rossby waves in the eastern part of the domain and eddy-eddy interactions in the west [Marshall, 1984]. The climatological double gyre circulation is not obvious from snapshots, only the western boundary current is predominant (Fig. 3.1d), when not masked locally by a rotational eddy flow. Especially at high resolution, instantaneous flow speeds may exceed 3 m/s, which is likely larger than maximum flow speeds observed in the global oceans. In the simulations regarded here, they usually occur between vortex dipoles (see Fig. 3.1c and f) and are therefore only of short durations. These findings do not change for runs with or without bottom friction.

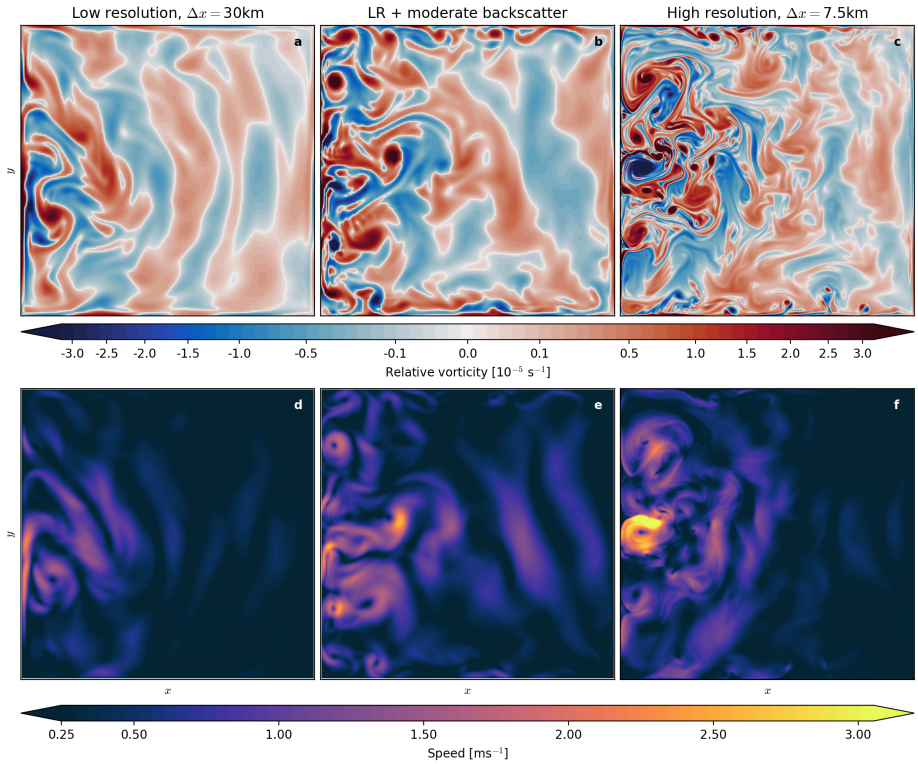

Figure 3.1: Snapshot of (a,b,c) relative vorticity and (d,e,f) speed after 30 years of integration for model runs with bottom friction. The time steps of (a,d), (b,e) and (c,f) are associated, respectively. Positive vorticity is associated with clockwise rotation and vice versa. Please note the non-linear colormap for relative vorticity to highlight non-extreme structures.

3.2 Reaching statistical equilibrium

In order to investigate the climatological mean of both the low resolution model and the high resolution truth, a spin-up phase is disregarded, which is not representative for a statistical equilibrium that is reached afterwards. We choose kinetic and potential energy (see equation 2.14) as a function of time to identify that a spin-up phase of 5 years is sufficient in that respect (Fig. 3.2). Furthermore, it is observed, that a higher resolution requires a longer spin-up phase. Simulations of very coarse resolution ($\Delta x > 60$km) reach their equilibrium state within weeks or months (not shown), presumably due to eddies not developing at such resolutions. It is likely that a higher level of kinetic and potential energy in the equilibrium state requires a longer spin-up

phase, such that also the bottom friction plays a crucial role: With bottom friction, the kinetic energy in the high resolution truth is approximately 100 kJm^{-2} (Fig. 3.2a), which is reached after 2 years, whereas switching off bottom friction yields almost three times higher levels of kinetic energy (Fig. 3.2b), that are only reached after 4 years of integration.

Due to the barotropic setting of the shallow water model (see section 2.1.1), the levels of potential energy are about one order of magnitude lower than those of kinetic energy. Using a gravitational acceleration of $g = 10\mathrm{m/s}$ in contrast to a reduced gravity in a baroclinic setting, the restoring force of the free surface η is much stronger, disabling large displacements from the undisturbed layer thickness H.

Comparing the energy levels between the low resolution model and the high resolution truth, we conclude that the model lacks energy in both its kinetic as well as its potential form by a factor of 2 to 3. Same relations between model and truth hold with and without bottom friction, respectively. Furthermore, bottom friction reduces the energy levels again by a factor of 2 to 3. Increased energy levels are also observed to conincide with enhanced long-term variability on multi-annual time scales, although seasons are absent from the shallow water model due to a time-constant wind forcing: In the high resolution truth without bottom friction, the level of potential energy is almost doubled from year 5 to 10 and from year 25 to 30 compared to other years (Fig. 3.2d). This kind of long-term variability is absent from the low resolution model, presumably due to lower levels of energy. However, this does not necessarily follow from altered ocean dynamics but can already be explained by integrating white noise in time with larger variance, which yields a larger variability simultaneously on all temporal scales.

3.3 Climatological mean state

Both, the low resolution model and the high resolution truth simulate in the time mean a double gyre circulation with (Fig. 3.3) and without bottom friction (Fig. 3.4) with a strong boundary current (e.g. the Gulf stream or Kuroshio in analogy to the real ocean) at speeds of about 1 m/s (Fig. 3.3c and i, and Fig. 3.4c and i). The southern (northern) gyre is referred to as sub-tropical (sub-polar) gyre. The low resolution model shows a weak inter-gyre gyre in the north-east corner, that reaches half-way to the west

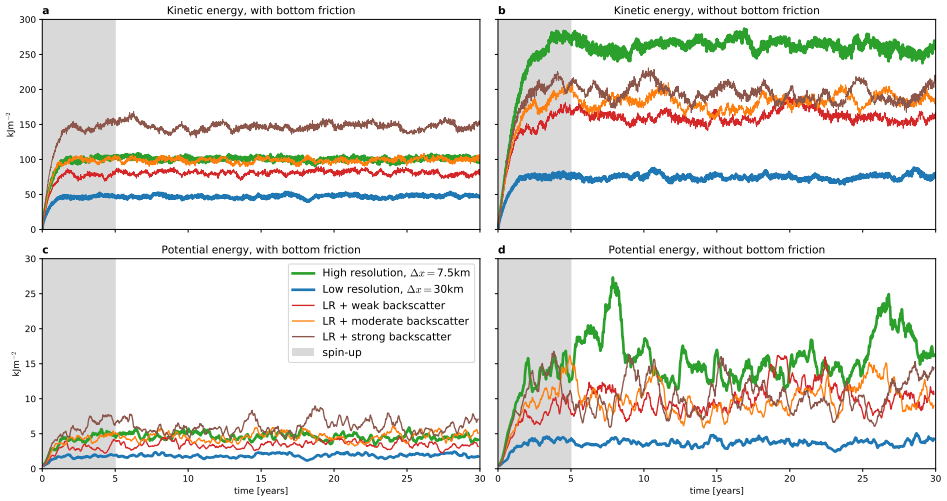

Figure 3.2: (a) Spatially integrated kinetic energy for 30-year long integrations of model runs as described in Table 2.1 with bottom friction. (b) as (a) but for model runs without bottom friction. (c) Potential energy for model runs with bottom friction, (d) as (c) but without bottom friction. Time series of potential energy are low-pass filtered with a running mean of window size of three months for clarity. The spin-up phase of 5 years is omitted for all analyses. Kinetic and potential energy is defined in equation 2.14.

(Fig. 3.3a and Fig. 3.4a). This inter-gyre gyre is more prolonged in the high resolution truth (Fig. 3.3g), especially without bottom friction (Fig. 3.4g). Having no bottom friction, a standing eddy develops in the north-west corner (Fig. 3.4g,h and i) that turns out to be much weaker without bottom friction (Fig. 3.3g,h and i) but is absent from all low resolution runs. Defining the across-basin current (e.g. the North Atlantic current in analogy to the real ocean) path as the mostly zonal zero-isoline of the surface displacement that reaches from the western boundary far into the east in our model runs, we observe at least some depedence on the resolution: At higher resolution and also higher energy levels (i.e. comparing with and without bottom friction) the across-basin current path is less undulated. This leads to the conclusion that any temperature bias in current global ocean or climate models [Flato *et al.*, 2013; Large & Danabasoglu, 2006] may already result from altered eddy dynamics due to a limited resolution.

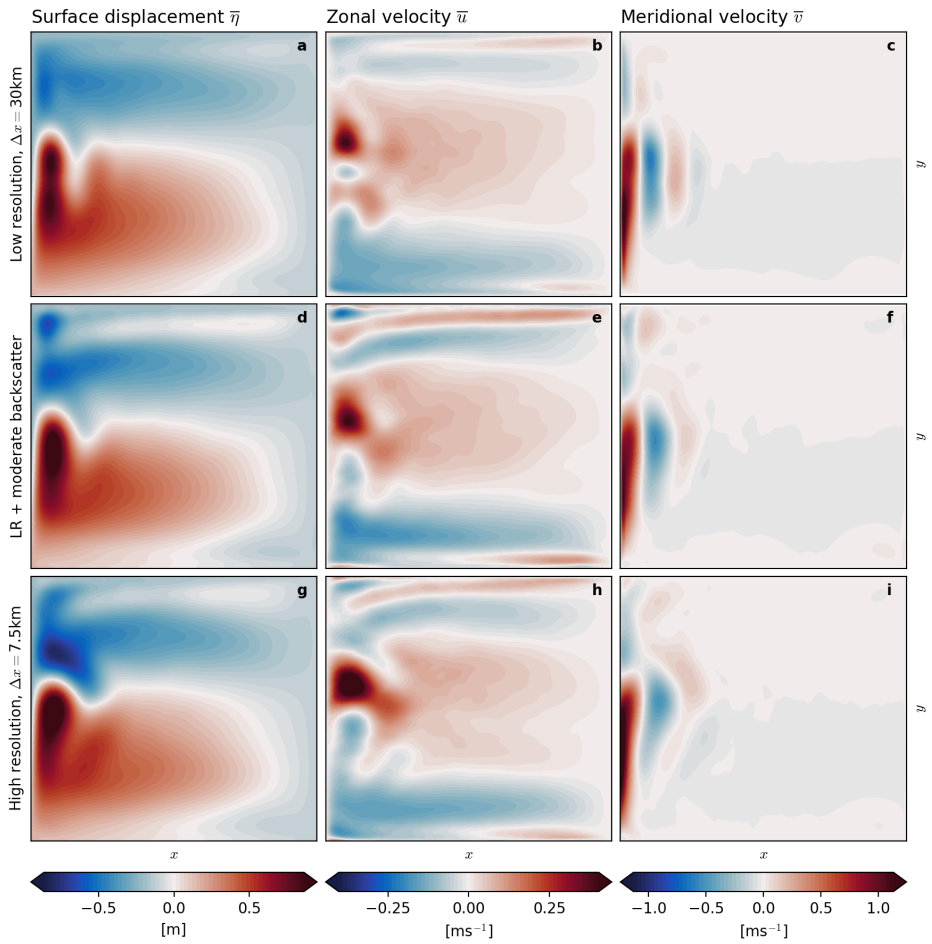

Figure 3.3: Climatological mean of the prognostic variables u, v, η for the model runs with bottom friction (see Table 2.1). The mean is calculated over 25 years, disregarding a spin-up of 5 years (see Fig. 3.2).

3.4 Energetics

As we have already seen in the previous section and especially in Fig. 3.2, the low resolution model simulates considerably lower energy levels, both kinetic and potential, compared to the high resolution truth. This section aims to understand this issue by regarding different energy reservoirs, namely mean kinetic energy (MKE, see equation 2.27), eddy kinetic energy (EKE), mean potential energy (MPE, see equation 2.26) and eddy potential energy (EPE) as well as the eddy kinetic energy spectrum and energy sources and sinks due to different terms in the energy equation (section 2.1.4).

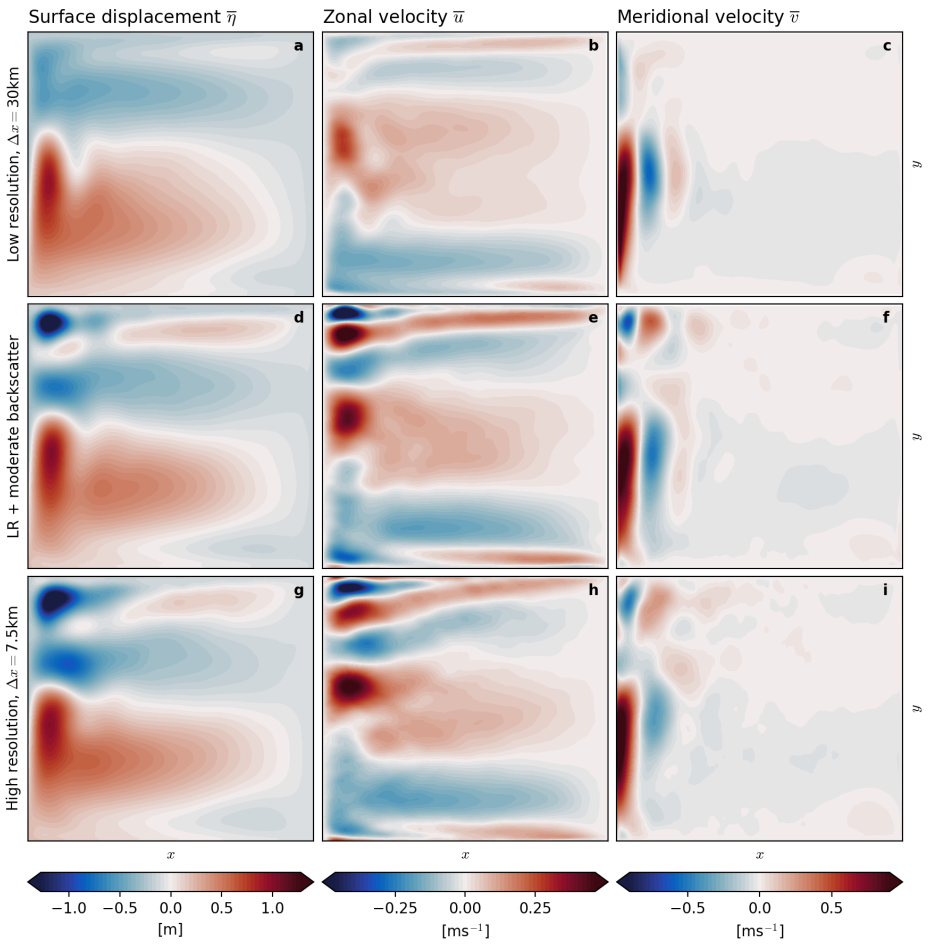

Figure 3.4: Same as Fig. 3.3 but for the model runs without bottom friction (see Table 2.1). Please note the different scaling of the color-shading.

Following the Reynolds decomposition into mean and anomalies (equation 2.23), we first point out that splitting kinetic and potential energy into its respective mean and eddy contribution refers to the time domain. In that respect, an eddy is a temporal anomaly and is not directly related to a spatially coherent structure with certain dynamics. Nevertheless, turbulence theory claims some similarities in the space and time domain, such that conclusions in one have some validity in the other [Palmer, 2012]. Keeping this in mind we carefully draw conclusions in the following analysis.

Both, the low resolution model and high resolution truth simulate high levels of MKE within the western boundary current, reaching into a weak

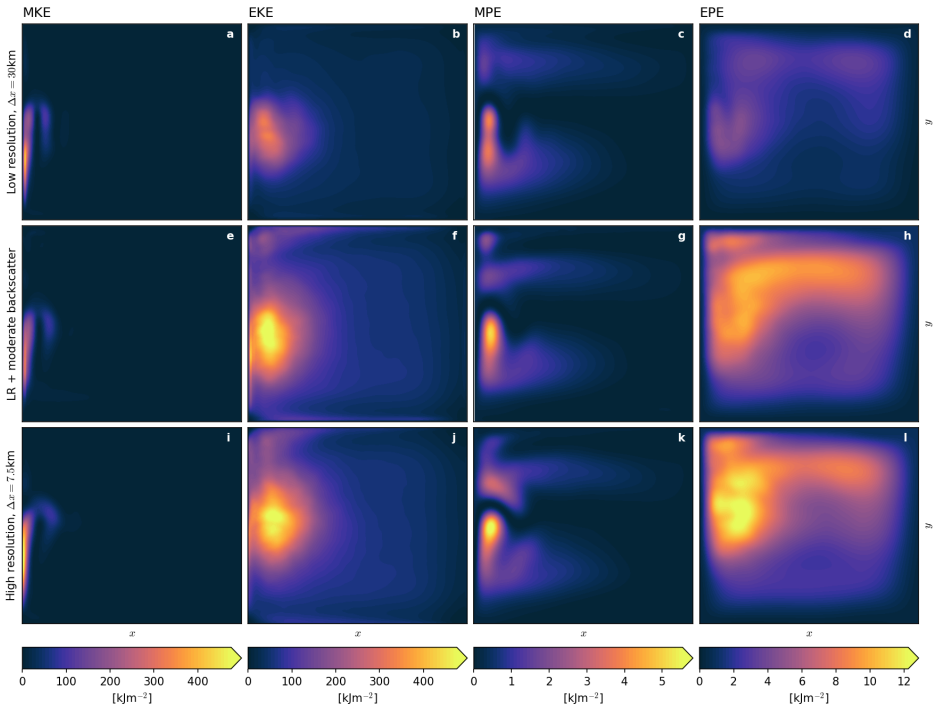

Figure 3.5: Climatological mean of mean kinetic energy (MKE), eddy kinetic energy (EKE), mean potential energy (MPE) and eddy potential energy (EPE) which are thickness-weighted as defined in equations 2.26 and 2.27. Shown are the model runs with bottom friction.

recirculation branch within the across-basin current (Fig. 3.5a and i). The same holds with and without bottom friction at comparable amplitude (Fig. 3.6a and i). This supports that only this part of the basin-wide circulation is a temporally prevailing current, whereas the flow in most other parts of the domain are either eddy-driven or caused by Rossby-waves but then negligible in strength. Consequently, there is a comparably enormous reservoir of EKE in the central western part of the domain, which is a factor of 2 to 3 larger in the high resolution truth compared to the low resolution model (Fig. 3.5b and j, and also without bottom friction in Fig. 3.6b and j). We therefore conclude that the lack of energy in the low resolution model compared to the high resolution truth is mostly due to lower levels of EKE and less so in terms of MKE. Similar conclusions hold for potential energy: MPE (Fig. 3.5c and k) follows mainly the climatogical mean of the surface displacement (Fig. 3.3a and i) with comparable amplitude but slightly different structure

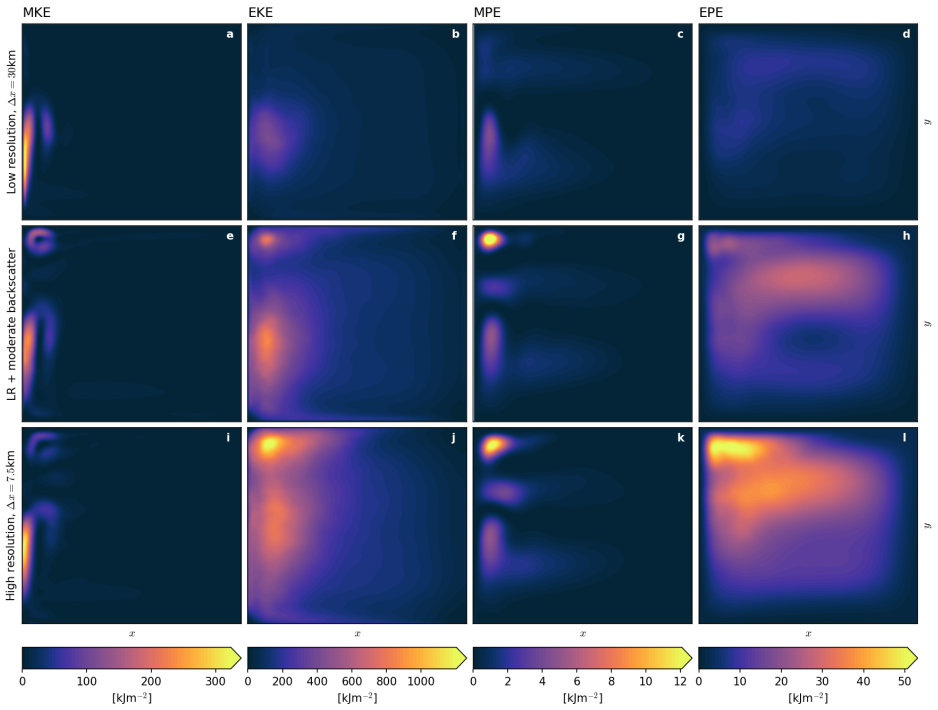

Figure 3.6: Same as Fig. 3.5 but for the model runs without bottom friction (see Table 2.1). Please note the different scaling of the color-shading.

due to the differences in the climatological mean circulation. In contrast, the EPE reservoir (Fig. 3.5d) is much larger than MPE (Fig. 3.5c) and spans throughout the northern part of the domain and especially pronounced in the central western part, where also EKE is found to be largest. Although similar in structure, the EPE reservoir is a factor of 2 to 3 larger in the high resolution truth (Fig. 3.5l) compared to the low resolution model (Fig. 3.5d).

This points towards the same conclusion: The low resolution especially lacks energy in the eddy contribution to kinetic and potential energy compared to the high resolution truth, which seems to be independent of bottom friction.

In order to understand the differences in eddy energy that come with different resolution we analyse the energy sources and sinks of the different terms in the shallow water equations (eq. 2.1). Without wind forcing, lateral mixing of momentum and bottom friction the shallow water equations obey conservation of energy, so that starting from rest these terms must explicitly account for sources and sinks of kinetic and potential energy to explain the

initial accumulation of energy in the spin-up phase as well as the leveling off to a statistical equilibrium afterwards. Regarding the climatological mean, where in the time-mean sense the amount of energy in the system is steady (Fig. 3.2), it is pointed out that all sources and sinks, once spatially integrated, must balance out. A local imbalance is compensated by the flow being able to propagate energy throughout the domain.

Wind forcing is found to be an energy source in large areas throughout the basin and an energy sink in others in both low resolution model and high resolution truth (Fig. 3.7a and d), which depends on the direction of the mean flow compared to the direction of the wind (see equation 2.16). Spatially integrated wind forcing is the only energy source to the shallow water system in the physical setting regarded here, and additionally largely independent of the resolution. The power due to the lateral mixing of momentum term altering the energy budget (Fig. 3.7b and e) reveals an energy sink in the eddy-dominated central western part of the domain, which is strong in the low resolution control but much weaker in the high resolution truth. The lateral mixing of momentum in connection with no-slip boundary conditions also removes lots of energy from the boundary. Due to the operator being biharmonic and therefore not sign-definite (see section 2.1.4) some of the energy that is removed right at the boundary is partly reinjected a grid cell or two farther away. Bottom friction removes energy largely from the western boundary current and the across-basin current being its extension, as flow speeds are fastest here. The pattern therefore resembles that of MKE (Fig. 3.5a and i). The energy removal due to bottom friction is slightly larger in the high resolution truth than in the low resolution model.

It is hence concluded that the effect of the lateral mixing on the energy budget is resolution dependent: Having a larger viscosity coefficient at coarser resolution yields a larger dissipation, that is usually understood as spuriously high compared to the real ocean, but necessary for numerical stability [Griffies & Hallberg, 2000].

Although the biharmonic lateral mixing of momentum is known to remove energy at the grid scale [Jansen & Held, 2014; Jansen *et al.*, 2015], it affects all spatial scales as seen in the EKE spectrum (Fig. 3.8). Most EKE is concentrated on spatial scales of the Rossby deformation radius with a power law decrease towards the grid scale being close to K^{-3}, pointing to a clearly developed turbulence cascade over a wide range of scales. Only with bottom

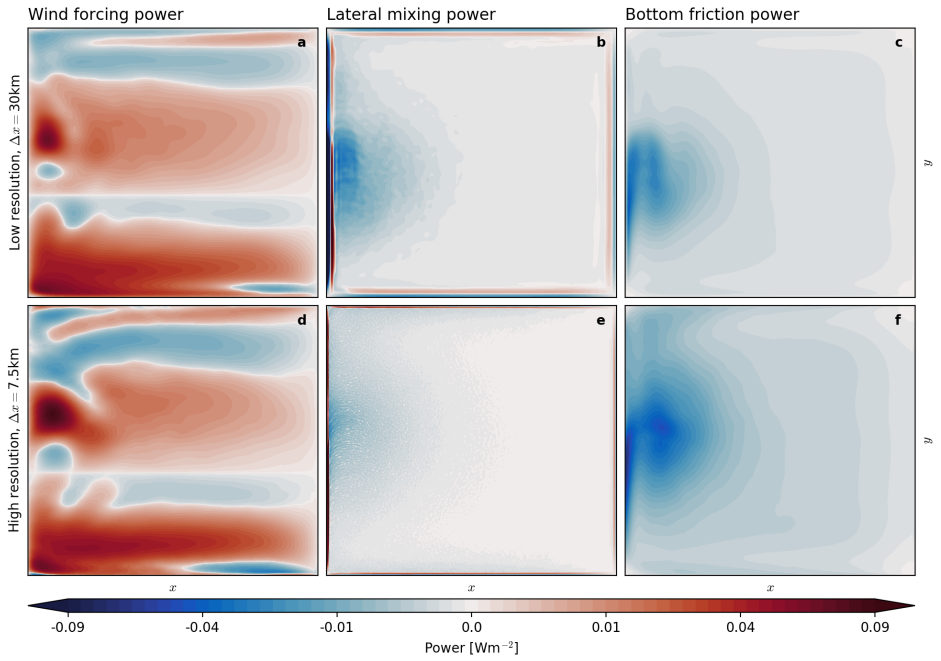

Figure 3.7: Climatological mean of energy sources and sinks due to wind forcing, lateral mixing of momentum and bottom friction for the two control runs without backscatter parametrization: (a,b,c) low resolution and (d,e,f) high resolution (see Table 2.1) with bottom friction. The power of the different terms is given in equations 2.16, 2.22 and 2.18. Positive values indicate an energy source and negative an energy sink to the system. Please note the non-linear colormap for visualization purposes.

friction the high resolution truth shows a slightly less steep descent, which is supported by other studies [Capet *et al.*, 2008]. Bottom friction is found to remove energy by a factor of about three from the largest scales, leaving the smaller scales mostly unaffected (compare Fig. 3.8a with b). This relates to removing energy from the largest eddies, which are responsible for the fastest flow speeds (Fig. 3.1d and f). From the perspective of the EKE spectrum it is concluded that for a successful parametrization it is necessary to either decrease the dissipation in the low resolution model or to reinject energy, such that spectral fluxes spread it across scales, in order to increase the EKE level.

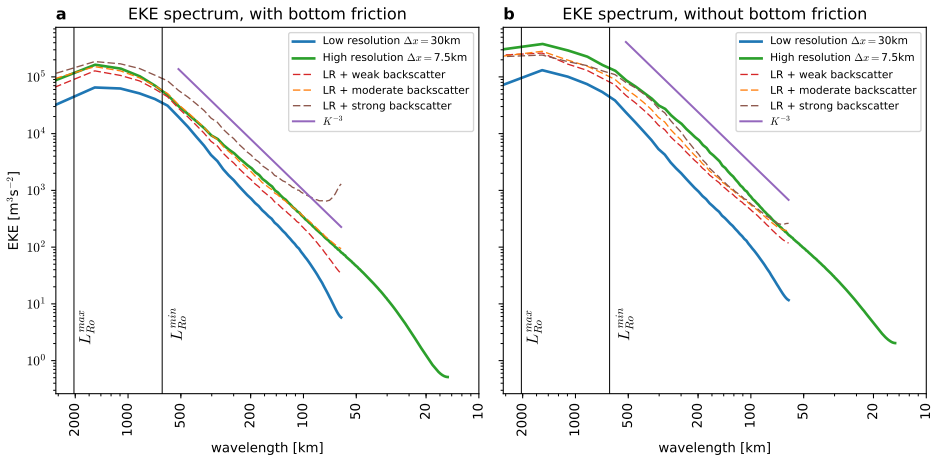

Figure 3.8: (a) Eddy kinetic energy spectrum for the model runs with bottom friction and (b) without (see Table 2.1). A theoretical spectrum of K^{-3} is given for comparison. The spectral energy is logarithmically plotted against horizontal wavenumber K but for readability relabelled with the corresponding wavelength. The Rossby radii of deformation $L_{R_o}^{\max}, L_{R_o}^{\min}$ (equation 2.45) are given for orientation.

3.5 Physical regime

To understand the difference between the low resolution model and the high resolution truth we furthermore investigate the physical regime in terms of Rossby and Reynolds numbers of these simulations. Both, Rossby and Reynolds numbers are directly calculated from the size of the terms in the shallow water equations 2.1 for every grid cell and every available time step as described in section 2.3. Distributions of Rossby and Reynolds numbers are shifted towards smaller values in the low resolution model compared to the high resolution truth (Fig. 3.9). Also bottom friction decreases the Rossby numbers, but has almost negligible effect on the Reynolds numbers. Rossby numbers follow approximately a log-normal distribution, as they are visibly normal distributed when plotted logarithmically on the abcissa. Similar for Reynolds numbers, whose distribution is a bit more skewed, with a fatter tail at low values (Fig. 3.9b and d). Low resolution model and high resolution truth both simulate a wide range of Rossby and Reynolds numbers: The 2.5th and 97.5th percentile span roughly two orders of magnitude for Rossby numbers and three to four orders of magnitude for Reynolds numbers.

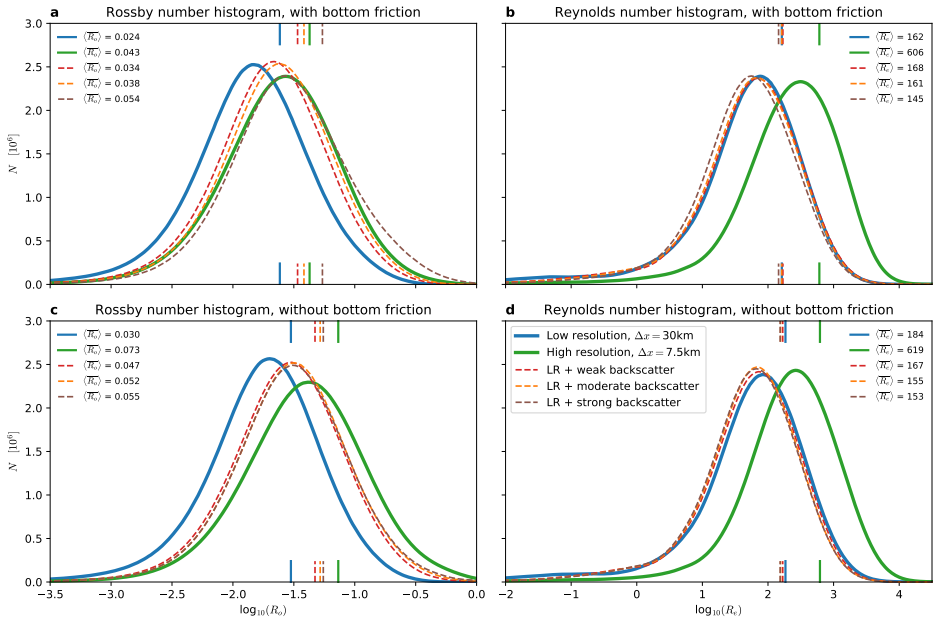

Figure 3.9: Rossby and Reynolds number histogram for (a,b) model runs with bottom friction and (c,d) model runs without bottom friction. For model runs with backscatter the effective Reynolds number R_e^* is used. Please note that histograms are plotted against the logarithm of Rossby and Reynolds number. Details can be found in section 2.3. Time and spatial mean Rossby and Reynolds numbers $\langle \overline{R_o} \rangle, \langle \overline{R_e} \rangle$ are marked as vertical ticks for all model runs in corresponding line styles and colors. Values are given in a second legend.

It is concluded that the low resolution model is not able to reproduce the turbulent nature of the high resolution truth as Rossby numbers are lower by a factor of two and Reynolds numbers by a factor of three to four.

3.6 Time scales

The time scales of the simulations are investigated by means of the autocorrelation function of the prognostic variables u, v, η at two different locations, denoted as point A and point B (see Fig. 2.1). Point A is chosen to be within the western boundary current detachment region and coincides with regions of largest EKE and EPE (Fig. 3.5 and Fig. 3.6). Point B is in the central eastern part of the domain where flow speeds are on average slow and energy levels are small. Hence, point A is thought of to represent a turbulent

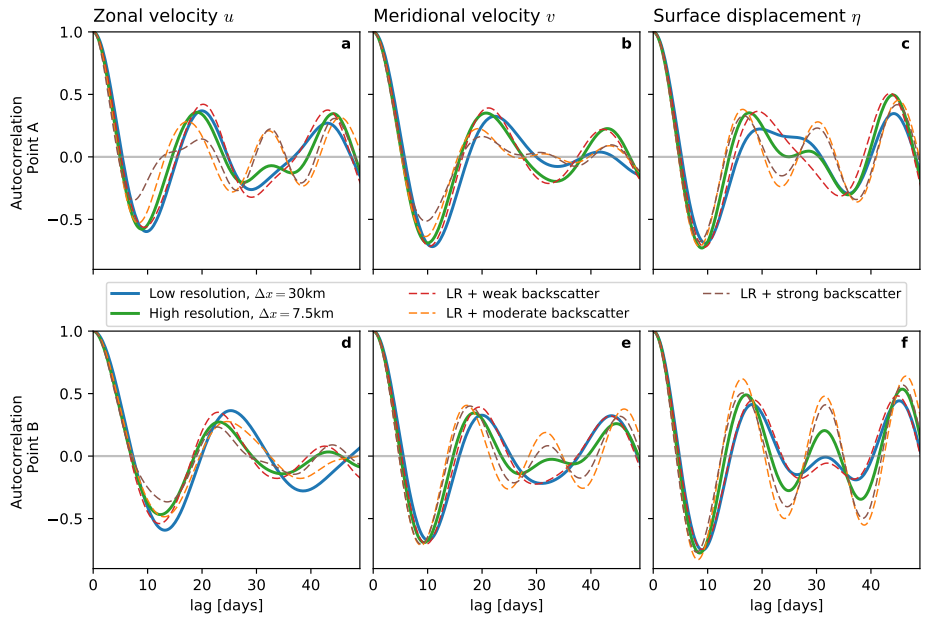

Figure 3.10: Autocorrelation function for the prognostic variables u, v, η of the model runs with bottom friction at point A (western boundary current detachment region) and B (central eastern part of the domain) as marked in Fig. 2.1.

and chaotic region, largely influenced by eddy dynamics. Point B in contrast should represent an area mainly driven by wave dynamics.

Although eddies are dominating the flow field at point A (Fig. 3.1), the autocorrelation clearly shows a reemerging signal after about 20 days in all prognostic variables (Fig. 3.10 and 3.11) pointing towards a less chaotic system, where an exponential decrease is expected [Cooper & Zanna, 2015]. Maximum anti-correlation is found after roughly 10 days with values exceeding -0.7, especially for surface displacement η. At high resolution, the time scales are observed to be shorter, as the autocorrelation function seems to be squeezed towards shorter lags. Increasing the resolution also increases the waviness of the autocorrelation function, especially without bottom friction at point B in v and η (Fig. 3.11e and f). Presumably due to a higher resolution, a less dissipative propagation of Rossby waves is enabled. Their signal is even clearly visible at point A, but more strongly masked due to eddies compared to point B.

The autocorrelation function is known to be in relation to the response to

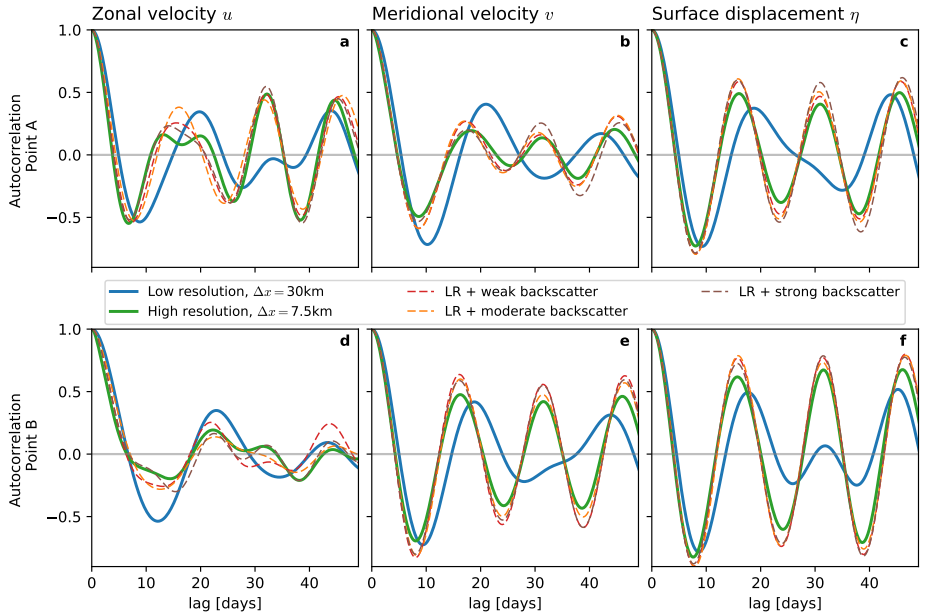

Figure 3.11: Same as Fig. 3.11 but for all model runs without bottom friction. See Table 2.1 for a list of all model runs.

forcing of a system. It is therefore also desired to improve the autocorrelation of the low resolution model towards the high resolution truth, which is important to correctly predict the system's adaptation e.g. to a climate change scenario [Cooper & Zanna, 2015]. The only forcing to a simple system as regarded here is the steady wind forcing, which could be intensified or weakend to investigate the systems response to that change in forcing. However, due to computational resources this analysis is not conducted, but the importance to simulate adequately the autocorrelation with a model is accentuated.

3.7 Lagrangian floats

We complete the analysis to understand differences between the low resolution model and the high resolution truth by investigating the spreading of Lagrangian floats in both simulations. The Lagrangian floats are released within the sub-tropical gyre close to the western boundary current as described in section 2.5. The release region is chosen as we expect the spreading of floats from the sub-tropical gyre to the sub-polar gyre to be largely dependent on

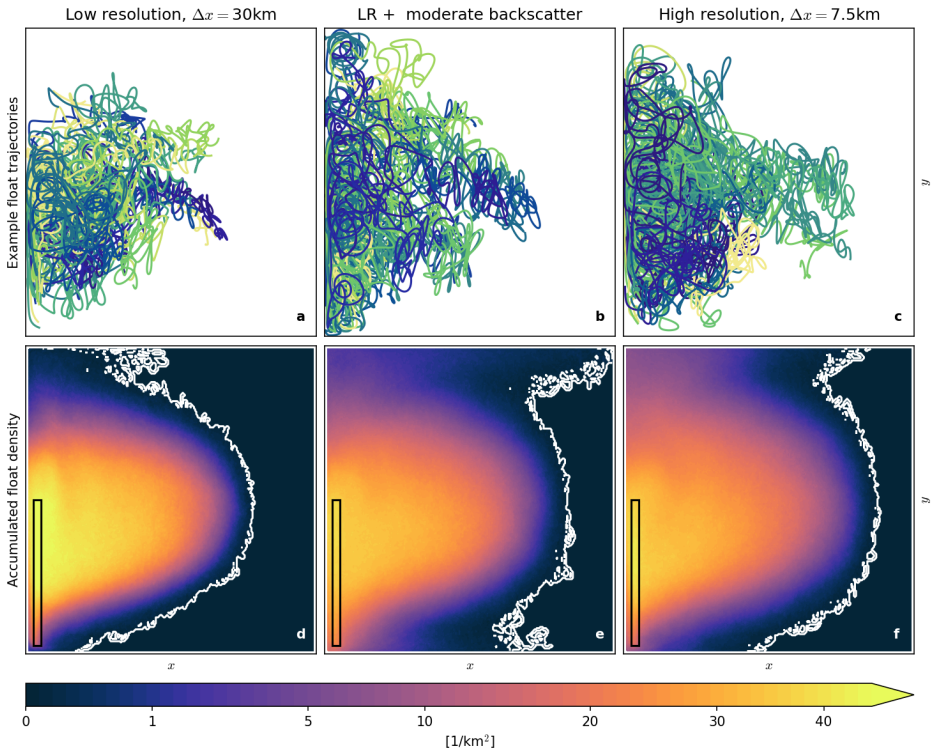

Figure 3.12: Lagrangian float trajectories (a-c) and accumulated float density (d-e) for the model runs with bottom friction. Details on the methodology are given in section 2.5. Floats are released in the black rectangle shown in (d-f). The trajectories in (a-c) represent 30 floats as an example and are randomly color-coded. The white line in (d-f) marks the zero-line of accumulated float density, hence the line that no float was able to cross within one year.

eddy-driven flow and therefore presumably different in the low resolution model compared to the high resolution truth. Advection with the time-mean flow $\overline{u}, \overline{v}$ (Fig. 3.14, for $\overline{u}, \overline{v}$ see Fig. 3.3b,c,h and i) reveals the importance of eddies (and Rossby waves as they are also excluded in the time-mean flow) for floats to leave a small recirculation cell of the sub-tropical gyre. Only a minority of floats recirculates on a trajectory that reaches into the eastern part of the sub-tropical gyre.

The time scale for the advection of floats is chosen to be one year. This is motivated as a float, travelling with the mean current may cross the basin within the across-basin current at approximately 0.1m/s, as follows from a harmonic zonal mean of the time mean zonal velocity. For a basin width of $L_x = 3840$km this would require more than a year to reach the eastern

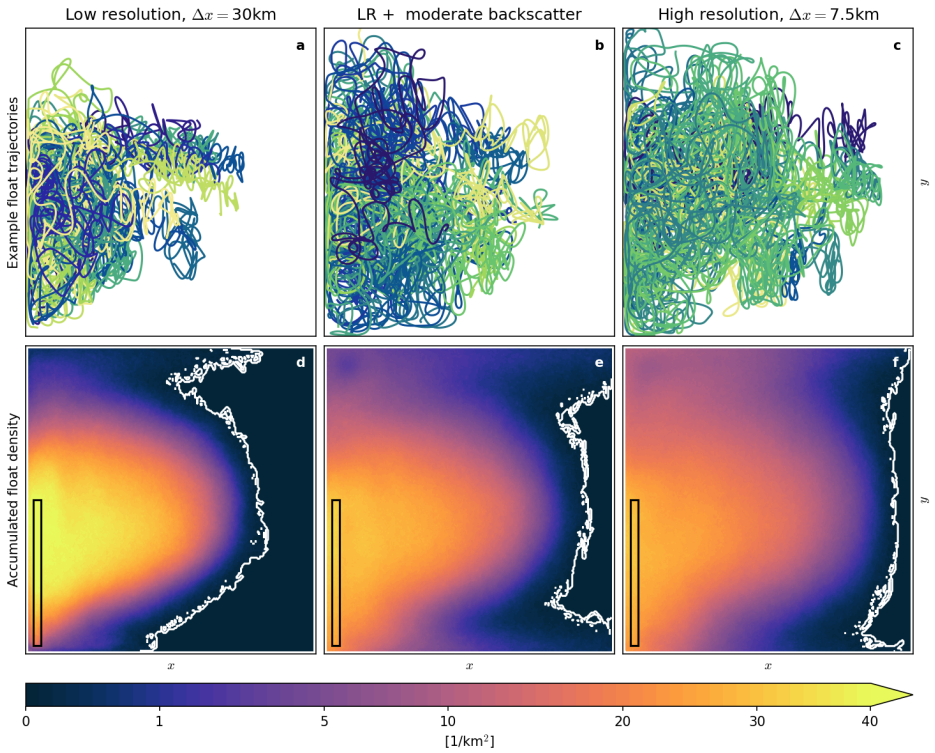

Figure 3.13: Same as Fig. 3.12 but for model runs without bottom friction.

boundary as supported by Lagrangian advection of the time-mean flow (Fig. 3.14).

Furthermore, we claim that the accumulated float density (for a definition see 2.5) is similar to a mean tracer concentration once certain requirements are given [Wagner, 2017]. This is explained in the following: Solving a tracer equation includes some tracer diffusion which is absent from a Lagrangian advection of floats. However, once eddies are resolved, the necessity for a large eddy diffusion coefficient is reduced. In this situation the stirring of the eddy-driven flow is much more effective in spreading the tracer than the mixing of the tracer by an explicit diffusion. A Lagrangian float does not experience the diffusion, but its trajectory is clearly dominated by eddies in our simulations (Fig. 3.12a,c and Fig. 3.13a,c), which supports the explicit eddy diffusion to be of minor importance. Furthermore, a tracer equation may include a source term that should resemble the characteristics of the float release region. Also, the time scale of a possible tracer sink term (i.e. a relaxation towards zero) that allows for a global statistical equilibrium

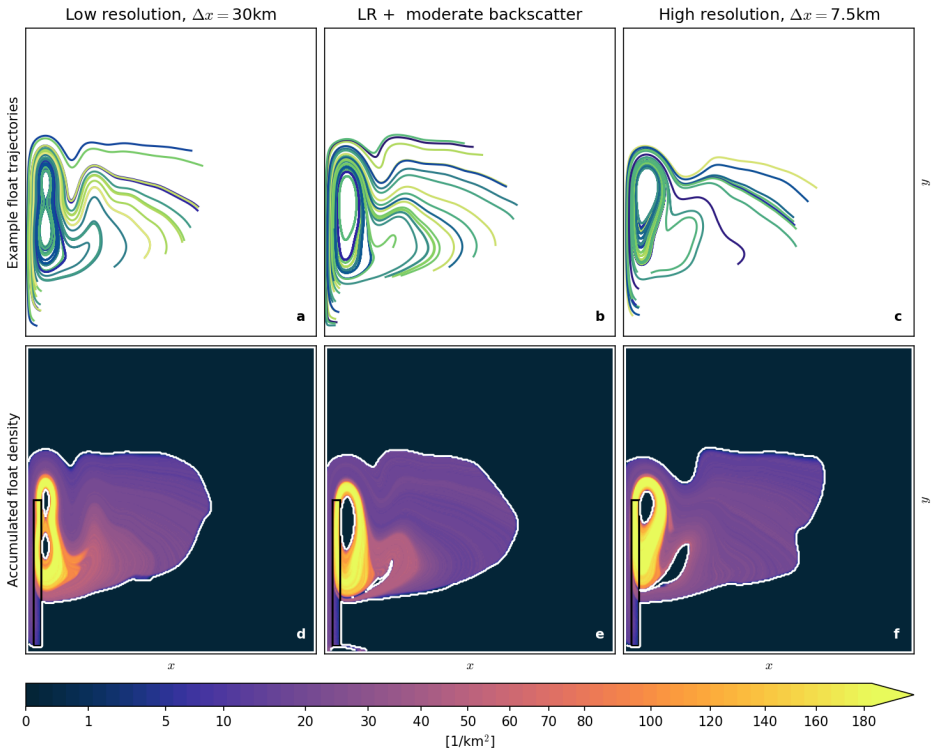

Figure 3.14: Same as Fig. 3.12 but for advection with the time-mean flow (Fig. 3.3b,c,e,f,h, and i).

concentration in presence of a source, should correspond to the length of the time period for which floats are advected. Summing up, keeping these constraints in mind, we expect the accumulated float density to lead to the same conclusion as we would draw from a mean tracer concentration.

In the low resolution model, the accumulated float density (Fig. 3.12d) reveals that most of the floats remain inside the sub-tropical gyre, only a few are able to enter the sub-polar gyre. However, within the sub-tropical gyre the floats are able to spread widely, which is contrast when only the time-mean flow is considered for advection (Fig. 3.14d). Accumulated float density in the high resolution truth shows that more floats are able to enter the sub-polar gyre (Fig. 3.14f), due to a better representation of eddies and small scale features: A negligible density of floats is apparent close to the northern boundary in the low resolution model which in the high resolution truth might be up to 25% of the density in the sub-tropical gyre. Furthermore, there is an increased number of floats that are able to move

against the mean current in the sub-tropical gyre in the proximity of the southern boundary, likely due to eddy transport (for a presence of eddies at the southern boundary see Fig. 3.1c). For neglecting bottom friction (Fig. 3.13), the same conclusions hold, but the floats tend to a more homogeneous spreading across the entire basin, such that the dominant feature of the accumulated float density is a west-east gradient. At high resolution and without bottom friction, floats are almost able to hit the eastern boundary (Fig. 3.13f).

We conclude that the spreading of a tracer or float may have some distinct differences dependent on how eddy-resolving the underlying simulation is. Areas that may not be easily accessible for a tracer or floats could be increasingly reached once eddies are sufficiently resolved. This is of special importance in ocean models including tracers, such as temperature, salinity or from biology or chemistry, where a mean tracer distribution may largely depend on the resolved eddy transport. Based on the results here, we draw the conclusion that large-scale biases in such tracer distributions may not be corrected simply by increasing the diffusion coefficient. Investigating the effect of an eddy parametrization on tracers or floats is therefore of relevance to improve global scale earth-system models.

3.8 Summary on model bias

In this section, we have seen how a low resolution model differs statistically from the high resolution truth that is taken as reference. Dependent on the resolution, it is necessary to alter the viscosity coefficient in the model (Table 2.1 and appendix A.2.6) to prevent numerical instabilities. This in turn changes the physical regime of the flow (section 3.5) and also leads to an increased dissipation (section 3.4) at the boundary as well as in the eddy-dominated region due an unrealistically high viscosity. A decreased eddy kinetic and potential energy budget follows, affecting the mean state (section 3.3), its variability (section 3.2) and the time scales of the flow (section 3.6). Experiments involving Lagrangian floats show how the effect of resolution projects onto a mean tracer distribution, which is of great importance in ocean circulation models involving temperature, salinity or other biological or chemical tracers.

As the resolution of climate models is limited by computational power,

we seek to parametrize the effect of eddies in the low resolution model as simulated by the high resoluton truth, instead of simply increasing the resolution. The approach taken here is referred to as energy-budget backscatter and is introduced in the following section.

Chapter 4

Energy budget-based backscatter parametrization

Based on the results of the previous chapter we seek to find a parametrization of eddies in the low resolution model in order to improve its statistics with respect to the high resolution truth. The approach taken here follows the energy budget-based backscatter [Jansen & Held, 2014; Jansen *et al.*, 2015], but is extended and applied to the shallow water model. Section 4.1 introduces the sub-grid EKE as prognostic variable. The newly formulated dissipation scaling based on the Rossby number is presented in section 4.2. The optimizing effect of the backscatter parametrization on the analyses of the previous chapter follows in section 4.3. Finally, section 4.4 summarizes the results of this chapter.

4.1 Sub-grid EKE as prognostic variable

The analyses of energy reservoirs of the previous chapter, including their sources and sinks, reveal that the low resolution model lacks eddy kinetic energy in comparison to the high resolution truth. This eddy kinetic energy is spuriously removed via viscosity not just in the vicinity of boundaries due to the no-slip boundary condition but also in the central western part of the domain where the majority of eddy mixing takes place. Following the idea of Eden & Greatbatch [2008] we therefore seek to keep track of the dissipated EKE from the resolved flow by transferring it into a sub-grid EKE budget. Hence, EKE is explicitly removed from the resolved flow, which is desirable

from a perspective of numerical stability [Griffies & Hallberg, 2000], but then added to an additional prognostic equation [Jansen & Held, 2014]. Assuming an upscale transfer of energy, in which the unresolved scales feed back to the resolved scales [Ferrari & Wunsch, 2009], a backscatter parametrization is formulated based on the local level of sub-grid EKE via negative viscosity. For details, the reader is referred to the methodology in section 2.2.

4.2 Dissipation scaling based on the Rossby number

The energy exchange term $\dot{E}_{\text{diss}}$ guarantees that the eddy kinetic energy, which is dissipated from the resolved flow by biharmonic viscosity, enters the prognostic equation for the sub-grid EKE e. In the original approach by Jansen *et al.* [2015] all dissipated eddy kinetic energy is transferred to the sub-grid EKE budget, that means Jansen *et al.* [2015] choose $c_{\text{diss}} = 1$ in equation 2.35. We therefore start by discussing the low resolution run with strong backscatter in the bottom friction case as this corresponds to the same choice. Based on the results of that model run we will advocate the necessity for altering the dissipation scaling c_{diss} and investigate its effect.

Without dissipation scaling, the dissipated energy gets eventually recycled and scattered back to larger scales via the backscatter term. This is equivalent to assuming a transfer of energy to larger scales, i.e. an upscale cascade. Keeping the dissipated eddy kinetic energy from the resolved flow in the sub-grid EKE budget allows the viscosity to mix momentum laterally but disables its energy and enstrophy dissipation. This is favourable in terms of numerical stability, which is largely dependent on the ability to mix momentum at the grid scale and hence to smooth gradients that are set up by numerical grid-scale oscillations [Griffies & Hallberg, 2000]. However, geostrophically balanced or unbalanced flows show a different behaviour in terms of spectral fluxes [Ferrari & Wunsch, 2009; Molemaker *et al.*, 2005]: A balanced flow exhibits a low Rossby number, pointing towards the importance of the Coriolis term in comparison to the advection term, and tends to undergo an upscale transfer of energy [Molemaker *et al.*, 2010; Scott & Wang, 2005]. In contrast, a geostrophically unbalanced flow, quantified by high Rossby numbers, favours a downscale transfer of energy, such that it is physically motivated to disable any recycling via the backscatter parametrization in

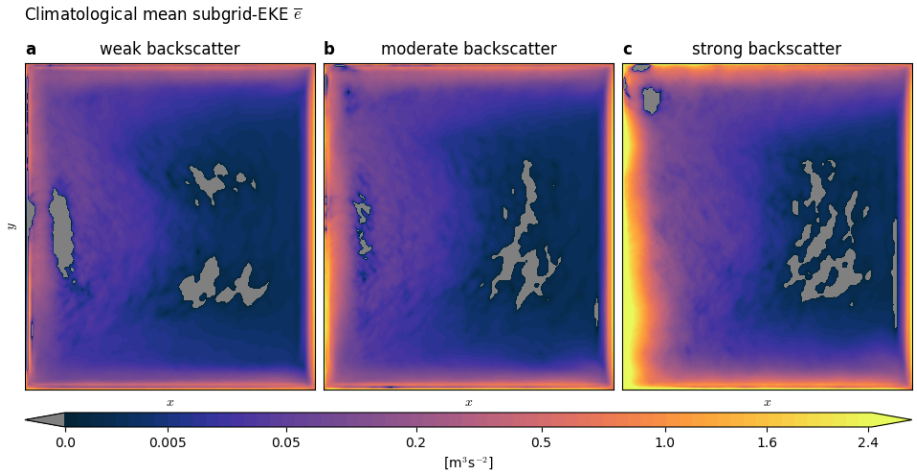

Figure 4.1: Climatological mean of the subgrid-EKE variable e for the low resolution model runs with (a) weak, (b) moderate and (c) strong backscatter and with bottom friction (see Table 2.1). Please note the non-linear colormap to highlight lower values. Grey areas have a negative subgrid-EKE as the biharmonic dissipation is not sign-definite (see discussion around equation 2.22) but are not accounted for in the backscatter term (see equation 2.34).

this case.

Having the no-slip boundary condition, it is important to understand that due to the strong shear flow at the boundary this is also the region where most of the energy is dissipated via viscosity [Zhai *et al.*, 2010]. Momentum of a boundary-parallel flow is mixed towards the boundary such that energy is dissipated in the proximity. Consequently, feeding the sub-grid EKE especially at the boundary explains its maximum values in the climatological mean: Fig. 4.1f reveals that most sub-grid EKE is concentrated in the western boundary region, spreading weakly into the central western interior. This is on one hand due to the explicit diffusion of sub-grid EKE in its prognostic equation, on the other hand also following from a pronounced EKE dissipation via viscosity where eddy mixing between the sub-tropical and sub-polar gyre (Fig. 3.7b) takes place.

The source of energy to the resolved flow via the backscatter parametrization increases with the local level of sub-grid EKE (see equation 2.34). It follows therefore that the backscatter parametrization corresponds to a forcing of the momentum equations at the boundary in our settings with the no-slip boundary condition. Regarding the EKE spectrum of the original

approach by Jansen *et al.* [2015], numerical oscillations at the grid scale are predominant which can be seen as the spectral energy increases close to the grid scale instead of decreasing linearly with about K^{-3} (Fig. 3.8a, brown dashed line). Snapshots, especially of relative vorticity, reveal that these numerial oscillations occur close to the boundary (not shown), so that we conclude that it would be favourable to decrease the strength of the backscatter parametrization locally.

Summing up these ideas concerning a dissipation scaling, we come up with a flow-aware c_{diss} parameter that depends on the Rossby number (see section 2.2), such that the dissipated energy of a high Rossby number-flow passes the sub-grid EKE budget and is not subject to recycling via the backscatter term. Having said that, the dissipated energy of a low Rossby number-flow still undergoes an upscale transfer as supported by the backscatter parametrization. Furthermore, it is pointed out that the dissipation scaling enables the model runs without bottom friction to remain numerically stable. This is not the case for the original approach by Jansen *et al.* [2015], as the overall dissipation within the shallow water system without bottom friction is too weak and leads to an increase of energy beyond realistic levels. The dissipation scaling acts therefore as an additional sink of energy, which is highly flow- and scale-dependent. This influences also the energy within the sub-grid EKE, lowering values especially in the proximity of the western boundary (Fig. 4.1a and b).

The direct Rossby number (equation 2.41) is large (i.e. $R_0 > 0.1$) in the vicinity of eddies, with maxmimum values in their centres, and associated filamentary flow structures (Fig. 4.2a). The Rossby number estimate R_o^* based on the deformation rate (see equation 2.43) is of similar structure and amplitude compared to the direct Rossby number, but includes high values for strong shear flow at the boundary (Fig. 4.2b). The resulting c_{diss} parameter for dissipation scaling therefore directly dissipates high Rossby number-flow within the western boundary current and detaching eddies but enables a recycling of the dissipated eddy kinetic energy elsewhere (Fig. 4.2c). Hence, we observe the dissipation scaling to converge to the original Jansen *et al.* [2015] approach for low Rossby numbers.

The only considered parameter for tuning in this novel approach is a non-negative scalar n_{diss}. For a choice of $n_{\text{diss}} \to 0$, this converges to the origial Jansen *et al.* [2015] approach and consequently larger values decrease

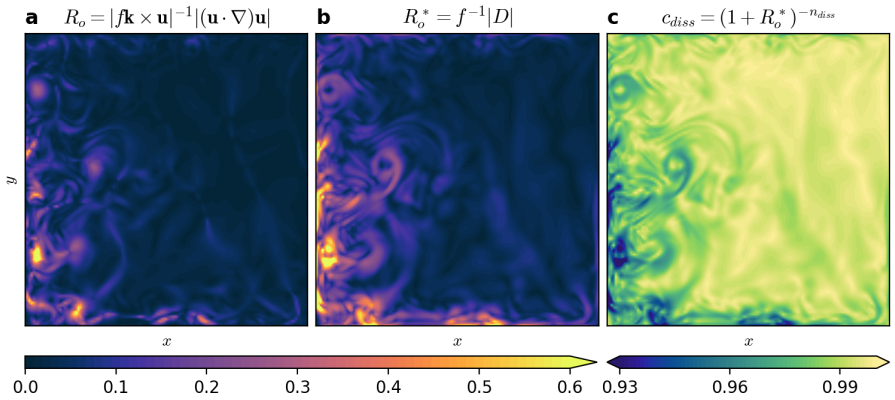

Figure 4.2: Snapshot of (a,b) Rossby numbers R_o, R_o^* and (c) the corresponding c_{diss} parameter from the low resolution run with bottom friction and moderate backscatter (same time step as in Fig. 3.1b,e). The definition of the Rossby numbers is given in equation 2.41 and 2.43, the c_{diss} parameter follows equation 2.31.

the backscatter strength. We find for $n_{\text{diss}} > 1$, the effect of the backscatter to be negligible, such that the low resolution run with backscatter converges towards its unparametrized control run. In the following, we will investigate the effect of varying n_{diss} within a subjectively chosen range and separate three cases: weak, moderate and strong backscatter for model runs with and without backscatter, respectively (see Table 2.1). We have to admit, that the respective backscatter strength does not correspond to each other when comparing model runs with and without bottom friction. Instead, the separation into weak, moderate and strong should be regarded in a relative sense. This is especially clear when regarding energy levels in the EKE spectrum (Fig. 3.8), as the energy increase from weak to moderate and from moderate to strong backscatter is different with and without bottom friction.

4.3 Improvements by the backscatter parametrization

The backscatter parametrization increases the levels of potential and kinetic energy compared to the unparametrized low resolution control run. Having bottom friction, the energy in the original Jansen *et al.* [2015] approach without dissipation scaling is clearly beyond the high resolution truth (denoted

as strong backscatter in Fig. 3.2a and c), justifying the requirement of an additional energy sink via the dissipation scaling, hence decreasing the strength of the backscatter parametrization. In contrast, backscatter of moderate strength results in energy levels and long-term variability that are virtually indistinguishable from the high resolution truth. This is different for the model runs without bottom friction: Here, even the strong backscatter is not able to reach the energy levels of the high resolution truth (Fig. 3.2b and d), as overall dissipation is too weak and eddy kinetic energy begins to pile up at the grid scale (Fig. 3.8b, brown dashed line) leading to numerical oscillations at the grid scale, especially visible in relative vorticity (not shown).

Regarding the energy levels, we conclude that without bottom friction the low resolution model is already close to the edge of numerical stability, limiting the ability of the backscatter parametrization to improve energy levels further towards the high resolution truth. In contrast, bottom friction reduces energy levels such that there is a larger potential for the backscatter parametrization to reinject the dissipated energy before reaching the edge of numerical stability. The increased energy levels due to the backscatter are almost entirely found in eddy kinetic and eddy potential energy, reproducing well the amplitude and spatial pattern of the high resolution truth (Fig. 3.5). Without bottom friction, amplitudes of EKE and EPE are not quite reached, in agreement with results from energy time series (Fig. 3.2).

Concerning the climatological mean state (Fig. 3.3), the backscatter parametrization is able to reproduce the sub-polar inter-gyre gyre, which was absent from the low resolution model without parametrization. However, the improvements concerning the mean state are much greater regarding the case without bottom friction (Fig. 3.4): Many structures reappear, that were absent from the unparametrized low resolution model, such that the climatological mean state is largely improved and almost identical to the high resolution truth. The role of bottom friction and its effect on the backscatter parametrizations remain unclear from the present analysis. The improvements of the climatological mean also project onto MKE and MPE (Fig. 3.5 and Fig. 3.6) seen in the similarity of spatial patterns.

With backscatter parametrization the low resolution model permits higher Rossby numbers and shifts their distribution towards that of the high resolution truth (Fig. 3.9a and c). Only the strong backscatter parametrization in the case with bottom friction outreaches the truth at high Rossby numbers

($R_o > 0.1$) although other parts of the distribution are reproduced well. However, the backscatter parametrization has almost negligible effect on the distribution of Reynolds numbers, although the effective Reynolds number R_e^* (equation 2.39) is considered. The distribution of Reynolds numbers is weakly shifted away from the high resolution truth, pointing towards a statistic that is not improved by the backscatter parametrization. Reasons for that remain unclear and are beyond the scope of this study.

The autocorrelation function of the high resolution truth is greatly reproduced once the backscatter parametrization is used in the low resolution model without bottom friction (Fig. 3.11). However, with bottom friction the improvements are not as clear (Fig. 3.10). This supports the previous findings that the role of bottom friction in relation to the backscatter parametrization is not easy to understand.

Presumably due to the higher levels of eddy kinetic energy we find the spreading of Lagrangian floats greatly improved by the backscatter parametrization (Fig. 3.12 and 3.13): Especially the spreading into the sub-polar gyre and against the mean current in the proximity of the southern boundary as observed in the high resolution truth is well reproduced.

4.4 Summary on backscatter parametrization

Summing up, we conclude that the backscatter parametrization as originally presented by Jansen *et al.* [2015] is inappropriate in the shallow water model settings used in this study: (i) Having a western boundary current and the no-slip boundary condition, the backscatter parametrization yields spurious numerical oscillations pointing to a too weak dissipation at the boundary. (ii) Without bottom friction, the shallow water model with backscatter parametrization is numerically unstable as the overall dissipation is too weak. We therefore present a dissipation scaling approach, that is based on the local Rossby number and thus highly flow- and scale-aware. This introduces another energy sink as the dissipated EKE from the resolved flow only partly enters the sub-grid EKE budget. This approach was shown to be very useful to remove numerical oscillations that otherwise occur at the grid scale. The low resolution model is largely improved in terms of eddy kinetic and potential energy leading to a better climatological mean and variability. Furthermore, the backscatter parametrization allows an

enhanced simulation of the physical regime (in terms of Rossby numbers), time scales and the spreading of Lagrangian floats. However, some aspects on the relation between the backscatter parametrization and bottom friction remain unclear and are not further investigated in this study.

Chapter 5

Concluding discussion

5.1 Discussion

The original Jansen *et al.* [2015] parametrization is shown to lead to a spurious excess of eddy kinetic energy at the grid scale in the vicinity of strong boundary currents with no-slip boundary conditions. In contrast, the parametrization presented in this study introduces a Rossby number-based dissipation scaling that yields an additional energy sink for geostrophically unbalanced flow [Ferrari & Wunsch, 2009; Molemaker *et al.*, 2010; Rhines, 1979]. We are thus able to overcome the numerical distortions at the western boundary that would otherwise limit the practicability of the backscatter parametrization.

The eddy-mean flow interaction in a low resolution model is shown to be largely enhanced, enabling the model to simulate an improved climatological mean, that presumably results from increased levels of eddy kinetic and eddy potential energy due to a more sophisticated simulation of the energy cycle. A positive impact on other statistics of the simulated flow is shown: Larger and therefore more realistic Rossby numbers are allowed to develop in the low resolution model; autocorrelation-based time scales are improved, pointing towards a more realistic response to forcing of the model; and Lagrangian floats have an increased ability to move against the mean current and across gyres by eddy-induced transport as observed in the high resolution truth.

However, the shallow water model considered here lacks in many aspects a comparability with the real ocean. Most importantly, only the vertically integrated sub-grid EKE is considered. It remains an open question how to

parametrize vertical fluxes of EKE in a more advanced three dimensional ocean general circulation model. For the sake of simplicity, computational power and importance of horizontal scales, we have focussed here on the two dimensional shallow water equations, which we find adequate to simulate eddy-mean flow interactions as a predominant process in the spectrum of turbulence in the global oceans. An idealized ocean basin is considered, which represents a sub-tropical to sub-polar ocean basin as a quadratic domain without realistic coast lines or bottom topography. However, we claim that this does not influence the major results of this study as processes of geostrophic turbulence occur similarly in all ocean basins with variable coast lines and bottom topography [Verdiere, 2009].

For simplicity, we used a constant viscosity coefficient for the biharmonic lateral mixing of momentum. More sophisticated approaches exist [Griffies & Hallberg, 2000; Leith, 1967; Smagorinsky, 1963], promoting the use of a flow- and scale-aware non-linear viscosity coefficient in order to remove enstrophy from the grid-scale and satisfy numerical stability. We have neither investigated the effect of this on our simulations, nor the concurrence with the here proposed dissipation scaling. A Smagorinsky-like viscosity could bear similarities to the approach taken here, both pointing towards the need of a highly flow- and scale-selective route to a realistic dissipation in ocean models.

To assess the impact of the backscatter parametrization, the resolution of the reference simulations is chosen to represent an ocean circulation model at eddy-permitting resolution. The effect on models of 1° horizontal resolution or coarser therefore remains uninvestigated, which are still state-of-the-art climate models run extensively at many climate research centres throughout the world [Flato *et al.*, 2013]. It is possible, as discussed by Jansen *et al.* [2015], that the disability to simulate eddies also limits the potential for improvements with a backscatter parametrization as dissipation acts before eddies are able to develop. This may lead to a spurious structure of the sub-grid EKE budget, disabling the negative viscosity to increase eddy kinetic energy intensively.

The role of bottom friction in concurrence with the backscatter parametrization remains unclear from this study as it enables energy reservoirs to be in close resemblance with the high resolution truth but contradictorily leads to limited improvements in terms of the climatological mean state or

autocorrelation-based time scales. The investigation of this is left for future work, however, we assume this issue to be of negligible importance once a more realistic layered ocean model is considered with bottom friction only acting in the lowermost model layer.

5.2 Summary and conclusion

An energy budget-based backscatter parametrization for the unresolved scales in a shallow water model driven by double gyre wind forcing is presented. The parametrization is an extension to the original approach by Jansen *et al.* [2015] proposing to use biharmonic viscosity in combination with an additional deterministic forcing term formulated as negative Laplacian viscosity to represent backscatter of energy from unresolved scales [Jansen & Held, 2014]. The kinetic energy that is removed from the resolved flow enters the sub-grid EKE budget, which is introduced as a prognostic variable. A newly formulated Rossby number-based dissipation scaling allows for a realistic route to dissipation for geostrophically unbalanced flow as supported by theory and observations. Based on local levels of sub-grid EKE the previously dissipated energy is reinjected at larger spatial scales via the backscatter term, ensuring numerical stability through an artifical upscale transfer of energy and hence a closure for the energy cycle.

The backscatter parametrization presented in this study is shown to largely improve the considered circulation model, effectively improving the simulation equivalent to about a factor of two to four increase in resolution at negligible additional computational cost. Unfortunately, it does not follow directly, that the implementation of an energy budget-based backscatter parametrization in a global climate model is straightforward, but we provide evidence for its potential to largely improve weather and climate predictions. We therefore highly promote the use and further research on energy budget-based backscatter methods.

Finally, we want to accentuate the importance of closing the energy cycle in an ocean circulation model [Eden, 2016] for successful climate simulations and a better prediction regarding climate change. Understanding the routes to dissipation in geophysical turbulence is a major challenge in theory and observations and is an essential basis for sophisticated parametrizations of unresolved scales. The energy budget-based backscatter approach provides the

potential to implement realistic routes to dissipation in an ocean circulation model, which motivates further research towards an enhanced understanding and hence predictability of the climate system.

Appendix

A.1 Shallow water equation formulation for the numerical model

A.1.1 Boundary conditions

The boundary conditions used in the shallow water model (equations 2.1) are explicitly given in the following. The kinematic boundary condition states that there is no flow through the boundary, i.e.

$$u(x = 0) = u(x = L_x) = v(y = 0) = v(y = L_y) = 0. \tag{A.1}$$

Additionally, for numerical convenience, we require no gradient of η across the boundary, hence

$$\partial_x \eta(x = 0) = \partial_x \eta(x = L_x) = \partial_y \eta(y = 0) = \partial_y \eta(y = L_y) = 0, \tag{A.2}$$

The tangential velocity at the boundary should vanish, which is usually referred to as no-slip boundary conditions

$$v(x = 0) = v(x = L_x) = 0, u(y = 0) = u(y = L_y) = 0. \tag{A.3}$$

However, sometimes these equations are replaced by

$$\partial_x v(x = 0) = \partial_x v(x = L_x) = \partial_y u(y = 0) = \partial_y u(y = L_y) = 0, \tag{A.4}$$

which are called *free-slip* boundary conditions, omitting a flux of momentum through the boundary, which are here given only for completeness but not used in this study.

A.1.2 Reformulation with Bernoulli potential and potential vorticity

The prognostic variables in the shallow water equations 2.1 so far are u, v, η, however, as η only appears in gradients, also h can be used as prognostic variable. We can separate from the advective terms in equations 2.1a,b the spatial gradient of kinetic energy. In combination with the pressure gradient term we introduce the Bernoulli potential p as

$$p = \frac{1}{2}(u^2 + v^2) + gh \tag{A.5}$$

Furthermore, with the relative vorticity $\zeta = \partial_x v - \partial_y u$ the potential vorticity can be defined as

$$q = \frac{f + \zeta}{h} \tag{A.6}$$

and equivalent to the shallow water equations we have

$$\partial_t u = qhv - \partial_x p + F_x + M_x + B_x + \xi_x \tag{A.7a}$$
$$\partial_t v = -qhu - \partial_y p + F_y + M_y + B_y + \xi_y \tag{A.7b}$$
$$\partial_t \eta = -\partial_x(uh) - \partial_y(vh) \tag{A.7c}$$

which are the equations solved by the numerical model as described in Appendix A.2.

A.2 Discretization of the shallow water model

In the following we will describe the discretization of equation A.7 in space and time. This discretization is then implemented into a numerical model code that can be found at `www.github.com/milankl/swm` and forms the numerical shallow water model as used throughout this study.

A.2.0 Notation

Some remarks on the notation used to describe the discretization of the shallow water model.

Surrounding grid points A superscript arrow points in the direction relative to the grid point where an operation is evaluated. More clearly,

regarding a variable a at $\mathbf{x} = (x_a, y_a)$ somewhere in the middle of the domain away from the boundaries. Then,

$$b^{\leftarrow} = b|_{\mathbf{x}=(x_a-\frac{1}{2}\Delta x, y_a)}, \quad b^{\rightarrow} = b|_{\mathbf{x}=(x_a+\frac{1}{2}\Delta x, y_a)} \tag{A.8}$$

where b is a variable that sits on the grid that is shifted by $\frac{1}{2}\Delta x$ in x-direction, and

$$c^{\downarrow} = c|_{\mathbf{x}=(x_a, y_a-\frac{1}{2}\Delta y)}, \quad c^{\uparrow} = c|_{\mathbf{x}=(x_a, y_a-\frac{1}{2}\Delta y)} \tag{A.9}$$

where c is a variable that sits on the grid that is shifted by $\frac{1}{2}\Delta y$ in y-direction, and

$$d^{\nearrow} = d|_{\mathbf{x}=(x_a+\frac{1}{2}\Delta x, y_a+\frac{1}{2}\Delta y)}, \quad d^{\searrow} = d|_{\mathbf{x}=(x_a+\frac{1}{2}\Delta x, y_a-\frac{1}{2}\Delta y)} \tag{A.10a}$$

$$d^{\swarrow} = d|_{\mathbf{x}=(x_a-\frac{1}{2}\Delta x, y_a-\frac{1}{2}\Delta y)}, \quad d^{\nwarrow} = d|_{\mathbf{x}=(x_a-\frac{1}{2}\Delta x, y_a+\frac{1}{2}\Delta y)} \tag{A.10b}$$

where d is a variable that sits on the grid that is shifted by both $\frac{1}{2}\Delta x$ in x-direction and $\frac{1}{2}\Delta y$ in y-direction. The notation is therefore independent of the indexing. For the description of the advective terms (section A.2.4) we may relate grid points that are further away by

$$b^{\Leftarrow} = b|_{\mathbf{x}=(x_a-\Delta x, y_a)}, \quad b^{\Rightarrow} = b|_{\mathbf{x}=(x_a+\Delta x, y_a)} \tag{A.11}$$

and similar for $\Uparrow, \Downarrow$. The single arrow therefore represents a grid point that is either $(\pm n\Delta x, 0)$, $(0, \pm n\Delta y)$ or $(\pm n\Delta x, \pm n\Delta y)$, with $n = \frac{1}{2}$, away. Same for the double arrow, but with $n = 1$. This notation is logically extended for a triple arrow $\Uparrow\uparrow$ (i.e. $n = \frac{3}{2}$), and so on.

The operator stencils usually change close to the boundary due to boundary conditions. In order to treat these cases separately we introduce the following, index-independent notation: Call a grid node northern boundary (NB), western boundary (WB), southern boundary (SB) or eastern boundary (EB), when the evaluation of a stencil for that grid node involves unresolved variables, because they sit either outside the domain $\mathcal{D}$ or on the boundary, where they are given by the boundary conditions.

Note that there is an overlap of two adjacent boundaries that we call accordingly north-east corner (NE), north-west corner (NW), south-west corner (SW) or south-east corner (SE). This notation is unfortunately only

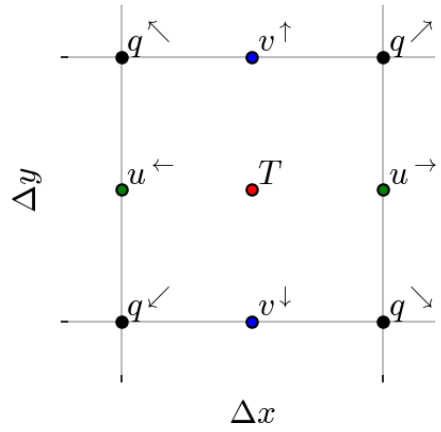

Figure 1: Illustrating the idea of an arrow-based notation for surrounding grid points. Here, the grid points around a grid point on the T-grid.

useful when stencils are small, but then provide a readable alternative.

Non-linear operations As the equations of interest are non-linear we cannot describe all operations in the model in terms of matrix-vector multiplications, additions of vectors or multiplications of a scalar with a vector. In fact, it turns out that all non-linear operations in equation (2.1), once discretized, are element-wise vector-vector multiplications. Let $\mathtt{a}, \mathtt{b}$ be two vectors of same length N, respectively element of a vector space V. Hence, they should sit on the same grid. We then define the element-wise vector-vector multiplication $*$ as

$$* : V \times V \to V, \mathtt{a} * \mathtt{b} \to \begin{pmatrix} a_1 b_1 \\ a_2 b_2 \\ \vdots \\ a_N b_N \end{pmatrix}, \quad \text{with } \mathtt{a} = \begin{pmatrix} a_1 \\ a_2 \\ \vdots \\ a_N \end{pmatrix}, \quad \mathtt{b} = \begin{pmatrix} b_1 \\ b_2 \\ \vdots \\ b_N \end{pmatrix} \tag{A.12}$$

and define the order of computation as inferior to matrix-vector multiplication, i.e.

$$\mathbf{A}\mathtt{b} * \mathtt{c} = (\mathbf{A}\mathtt{b}) * \mathtt{c} \neq \mathbf{A}(\mathtt{b} * \mathtt{c}) \tag{A.13}$$

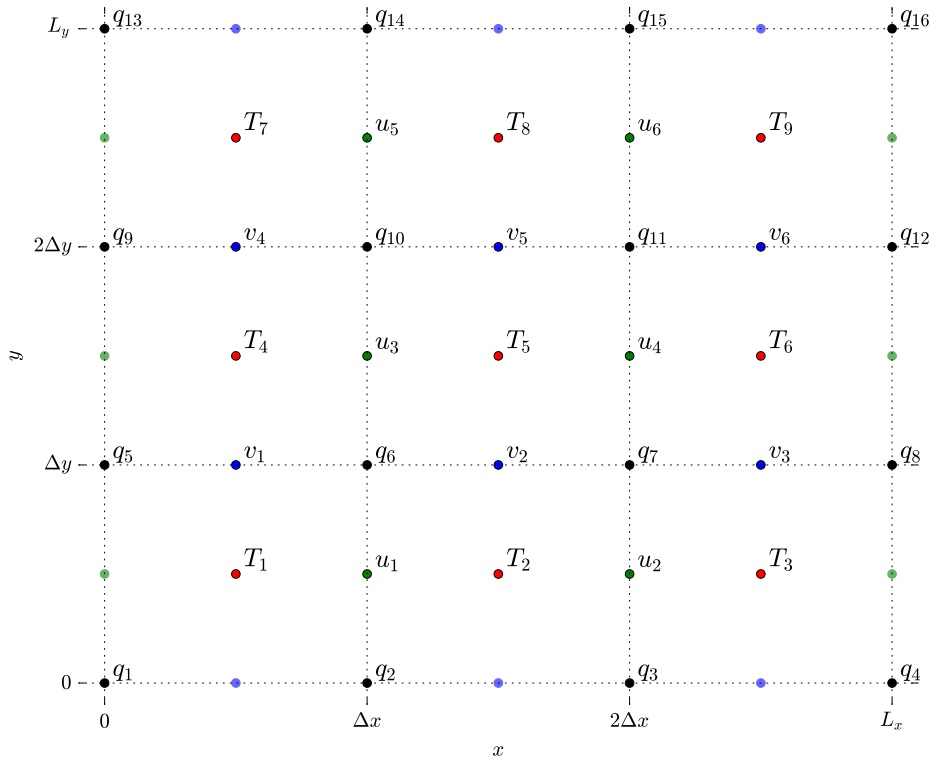

Figure 2: Row-first indexing on the Arakawa C-grid for an example grid with $n_x = n_y = 3$. The variables on the boundary as denoted by faint green and blue discs are not explicitly resolved but given by the boundary conditions. In contrast, the values of q in the corners (i.e. q_1, q_4, q_{13} and q_{16} here) are numbered for simplicity although always being 0 (also referred to as *ghost points*).

for all matrices $\mathbf{A}$, and vectors $\mathtt{b}, \mathtt{c}$. Furthermore, we write

$$\frac{1}{\mathtt{a}} = \begin{pmatrix} \frac{1}{a_1} \\ \frac{1}{a_2} \\ \vdots \\ \frac{1}{a_N} \end{pmatrix} \tag{A.14}$$

to denote the element-wise multiplicative inverse of $\mathtt{a}$.

A.2.1 Arakawa C-Grid

The domain $\mathcal{D}$ is divided into $n_x \times n_y$ grid cells, evenly spaced, so that each grid cell has the side length $\Delta x = \frac{L_x}{n_x}$ in x-direction and $\Delta y = \frac{L_y}{n_y}$ in y-direction. The total amount of grid cells is $n_x n_y$. Let the variable η_i sit in the middle of the i-th grid cell at position (x_i, y_i), i.e. $\eta_i = \eta(x_i, y_i)$. We use only one index i so that $i \in \{1, ..., n_x n_y\}$ in order to index all grid cells. We choose row-first indexing as in Fig. 2, which is used throughout the numerical model code.

Following the ideas of the Arakawa C-grid [Arakawa & Lamb, 1977, 1981], the discretization of the variables u, v and q is staggered. In general, we might use an independent indexing for u, v and q and therefore introduce $j, k, l \in \mathbb{N}$. We distinguish between 4 different grids: (i) the T-grid, for η, h, (ii) the u-grid, (iii) the v-grid, (iv) the q-grid. Not for all grid cells it is necessary to evaluate u or v, as they might vanish due to the boundary conditions. The grids therefore carry a different amount of grid points. Let N_T, N_u, N_v, N_q be the total number of grid points on the respective grids then

$$\begin{aligned} N_T &= n_x n_y, & N_u &= (n_x - 1) n_y \\ N_q &= (n_x + 1)(n_y + 1), & N_v &= n_x (n_y - 1) \end{aligned} \tag{A.15}$$

The n_x-th column of u-points vanish, as does the n_y-th row of v-points. However, there is no boundary condition for q, which makes it necessary to evaluate the q-grid for all points within the domain $\mathcal{D}$.

Choosing one index for the grid points leads to the advantage that every scalar variable can be represented as a vector with the following vector-representation $\mathtt{u}, \mathtt{v}, \mathtt{h}, \mathtt{q}$ of u, v, h and q

$$\mathtt{u} = \begin{pmatrix} u_1 \\ u_2 \\ \vdots \\ u_{N_u} \end{pmatrix}, \quad \mathtt{v} = \begin{pmatrix} v_1 \\ v_2 \\ \vdots \\ v_{N_v} \end{pmatrix}, \quad \mathtt{h} = \begin{pmatrix} h_1 \\ h_2 \\ \vdots \\ h_{N_T} \end{pmatrix}, \quad \mathtt{q} = \begin{pmatrix} q_1 \\ q_2 \\ \vdots \\ q_{N_q} \end{pmatrix}. \tag{A.16}$$

In the special case of $n_x = n_y$ the vectors $\mathtt{u}, \mathtt{v}$ are of same size, but in gen-

eral $\mathtt{u}, \mathtt{v}, \mathtt{h}, \mathtt{q}$ all differ in their sizes. Unfortunately, the vector-representation of the variables leads to complicated distinguishing between grid nodes that are in vicinity of the boundaries and those in the middle of the domain. In the following, we will evaluate the model variables on different grids and denote that with $\mathbf{x}_i$, $\mathbf{x}_j^u$, $\mathbf{x}_k^v$ and $\mathbf{x}_l^q$, which is short-hand for all grid points of the T-, u-, v- and q-grid, respectively.

A.2.2 Gradients

Matrix-Vector multiplication idea

Representing the model variables in vector-form, as discussed above, enables us to think of a gradient ∂ as a linear map between two vector spaces[1] V_1, V_2. Hence, any gradient ∂ in that sense can be written as a matrix $\mathbf{G}$ which is multiplied with a vector $\mathtt{z}$ representing one of the model's variables:

$$\partial : V_1 \to V_2, \mathtt{z} \to \mathbf{G}\mathtt{z} \tag{A.17}$$

Having 4 different grids, we have to deal with four different vector spaces V_u, V_v, V_T, V_q with dimensions N_u, N_v, N_T, N_q, respectively. In the following we will investigate the entries of $\mathbf{G}$ such that they describe centred finite differences on the four different grids. The same holds for any linear interpolation $\mathcal{I}$ from one grid to another as will be discussed in section A.2.3. We write then

$$\mathcal{I} : V_1 \to V_2, \mathtt{z} \to \mathbf{I}\mathtt{z} \tag{A.18}$$

Gradient operation as matrix multiplication

In the following we will use a notation where the subscript denotes the direction of the derivative, hence x or y, and the superscript u, v, T, q denotes the vector space, where ∂ is mapping from. For the x-derivative of h on the T-grid this is

$$\partial_x^T : V_T \to V_u, \mathtt{h} \to \mathbf{G}_x^T\mathtt{h} \tag{A.19}$$

and the result $\mathbf{G}_x^T\mathtt{h}$ sits then on the u-grid (as defined in equation A.21) or equivalently is element of the vector space V_u. The matrix $\mathbf{G}_x^T$ is therefore

[1] Strictly speaking, these are not vector spaces as the underlying algebraic field are not the real numbers but the set of computer representable numbers given a certain precision, e.g. 64bit. These are mathematically not an algebraic field, but for simplicity here regarded as an approximation to it.

of size $N_u \times N_T$ and so not a square matrix (see eq. A.15). The derivatives $\partial_y h, \partial_x u, \partial_y u, \partial_x v, \partial_y v, \partial_x q$ and $\partial_y q$ can similarly be written as

$$\partial_y^T : V_T \to V_v, \mathtt{h} \to \mathbf{G}_y^T \mathtt{h} \tag{A.20a}$$
$$\partial_x^u : V_u \to V_T, \mathtt{u} \to \mathbf{G}_x^u \mathtt{u} \tag{A.20b}$$
$$\partial_y^u : V_u \to V_q, \mathtt{u} \to \mathbf{G}_y^u \mathtt{u} \tag{A.20c}$$
$$\partial_x^v : V_v \to V_q, \mathtt{v} \to \mathbf{G}_x^v \mathtt{v} \tag{A.20d}$$
$$\partial_y^v : V_v \to V_T, \mathtt{v} \to \mathbf{G}_y^v \mathtt{v} \tag{A.20e}$$
$$\partial_x^q : V_q \to V_v, \mathtt{q} \to \mathbf{G}_x^q \mathtt{q} \tag{A.20f}$$
$$\partial_y^q : V_q \to V_u, \mathtt{q} \to \mathbf{G}_y^q \mathtt{q} \tag{A.20g}$$

All entries of the gradient matrices $\mathbf{G}$ follow from the equations A.21, A.22, A.23, A.24, A.25, A.29 and A.30 and are then only a matter of indexing.

Centred differences

Writing the scalar variables on a grid as vectors comes with the disadvantage, that the exact mathematical indexing gets rather complicated and lacks readability. We will therefore discuss the gradient and interpolation operations in the following only in terms of their stencil, i.e. the linear combination of the variables at the surrounding grid points that yields the desired result. To be a bit more precise and to include the treatment of the boundaries, we will use the notation described in section A.2.0.

Centred finite difference approximation of the gradient in x-direction of a variable η on the T-grid yields a result that sits on the u-grid and reads

$$\partial_x \eta|_{\mathbf{x}=\mathbf{x}_j^u} \approx \frac{\eta^{\rightarrow} - \eta^{\leftarrow}}{\Delta x} \tag{A.21}$$

This is the well-known $(-1, 1)$-stencil. The y-derivative of a variable of the T-grid sits on the v-grid:

$$\partial_y \eta|_{\mathbf{x}=\mathbf{x}_k^v} \approx \frac{\eta^{\uparrow} - \eta^{\downarrow}}{\Delta y} \tag{A.22}$$

The x-derivative of a variable on the u-grid includes the kinematic boundary conditions, hence a 0 appears for computations involving the boundary

nodes. The result sits on the T-grid:

$$\partial_x u|_{\mathbf{x}=\mathbf{x}_i} \approx \frac{1}{\Delta x} \begin{cases} u^{\rightarrow} - 0 & \text{if western boundary} \\ 0 - u^{\leftarrow} & \text{if eastern boundary} \\ u^{\rightarrow} - u^{\leftarrow} & \text{else.} \end{cases} \tag{A.23}$$

Similarly for the y-derivative on the v-grid which sits again on the T-grid:

$$\partial_y v|_{\mathbf{x}=\mathbf{x}_i} \approx \frac{1}{\Delta y} \begin{cases} v^{\uparrow} - 0 & \text{if southern boundary} \\ 0 - v^{\downarrow} & \text{if northern boundary} \\ v^{\uparrow} - v^{\downarrow} & \text{else.} \end{cases} \tag{A.24}$$

The discretization of $\partial_x q$ and $\partial_y q$ are in close relation to equation A.21 and A.22 and do not involve any boundary conditions

$$\partial_x q|_{\mathbf{x}=\mathbf{x}_k^v} \approx \frac{q^{\rightarrow} - q^{\leftarrow}}{\Delta x}, \quad \partial_y q|_{\mathbf{x}=\mathbf{x}_j^u} \approx \frac{q^{\uparrow} - q^{\downarrow}}{\Delta y} \tag{A.25}$$

Note, that some grid nodes of q on the boundary are simply not evaluated in this computation.

Implementing the tangential boundary conditions

For $\partial_y u, \partial_x v$ the tangential boundary conditions as no-slip (equation A.3) or free-slip (equation A.4) come into play. For simplicity we first look at $\partial_y u|_{\mathbf{x}=\mathbf{x}_l^q}$ for $l = 2$, i.e. at $\mathbf{x} = (\Delta x, 0)$, where the derivative is

$$\partial_y u|_{\mathbf{x}=(\Delta x,0)} \approx \frac{u_1 - u_b}{\Delta y} \tag{A.26}$$

with $u_b = u(\Delta x, -\frac{1}{2}\Delta y)$ the velocity just outside the domain if the grid where extend in negative y direction. To match the no-slip boundary condition (equation A.3) we set $u_b = -u_1$, so that at $\mathbf{x} = (\Delta x, 0)$, i.e. right on the boudary we have $u = 0$, when applying linear interpolation. This yields

$$\partial_y u|_{\mathbf{x}=(\Delta x,0)} \approx \frac{2u_1}{\Delta y} \tag{A.27}$$

In contrast, when choosing free-slip boundary conditions (equation A.4) we set $u_b = u_1$ for similar reasoning. Then

$$\partial_y u|_{\mathbf{x}=(\Delta x,0)} \approx \frac{0u_1}{\Delta y} = 0 \tag{A.28}$$

as desired. With introducing the parameter $\alpha \in \{0, 2\}$ Madec [2016] switch between no-slip ($\alpha = 2$) and free-slip boundary conditions ($\alpha = 0$). A choice of $0 < \alpha < 2$ corresponds to partial-slip. Following these ideas we write the y-derivative on the u-grid as

$$\partial_y u|_{\mathbf{x}=\mathbf{x}_l^q} \approx \frac{1}{\Delta y} \begin{cases} 0 & \text{if western or eastern boundary} \\ \alpha u^{\uparrow} & \text{if southern boundary without SW,SE} \\ -\alpha u^{\downarrow} & \text{if northern boundary without NW, NE} \\ u^{\uparrow} - u^{\downarrow} & \text{else.} \end{cases} \tag{A.29}$$

which sits then on the q-grid. Similarly we have the discretization of $\partial_x v$ as

$$\partial_x v|_{\mathbf{x}=\mathbf{x}_l^q} \approx \frac{1}{\Delta x} \begin{cases} 0 & \text{if northern or western boundary} \\ \alpha v^{\rightarrow} & \text{if western boundary without NW,SW} \\ -\alpha v^{\leftarrow} & \text{if eastern boundary without NE, SE} \\ v^{\rightarrow} - v^{\leftarrow} & \text{else.} \end{cases} \tag{A.30}$$

Higher order derivative at the boundary

Shchepetkin & O'Brien [1996] propose for no-slip boundary conditions ($\alpha = 2$) to use instead of equation (A.29), (A.30) the larger stencil $(4, -1, \frac{1}{5})$ at the boundary

$$\partial_y u|_{\mathbf{x}=\mathbf{x}_l^q} \approx \frac{1}{\Delta y} \begin{cases} 0 & \text{if western or eastern boundary} \\ 4u^{\uparrow} - u^{\Uparrow} + \frac{1}{5}u^{\Uparrow\uparrow} & \text{if southern boundary without SW,SE} \\ -4u^{\downarrow} + u^{\Downarrow} - \frac{1}{5}u^{\Downarrow\downarrow} & \text{if northern boundary without NW, NE} \\ u^{\uparrow} - u^{\downarrow} & \text{else.} \end{cases} \tag{A.31}$$

$$\partial_x v|_{\mathbf{x}=\mathbf{x}_l^q} \approx \frac{1}{\Delta x}\begin{cases} 0 & \text{if northern or western boundary} \\ 4v^{\rightarrow} - v^{\Rightarrow} + \frac{1}{5}v^{\overrightarrow{\Rightarrow}} & \text{if western boundary without NW,SW} \\ -4v^{\leftarrow} + v^{\Leftarrow} - \frac{1}{5}v^{\overleftarrow{\Leftarrow}} & \text{if eastern boundary without NE, SE} \\ v^{\rightarrow} - v^{\leftarrow} & \text{else.} \end{cases} \tag{A.32}$$

These operators will be called ${}^2\mathbf{G}_y^u$ and ${}^2\mathbf{G}_x^v$ (see next section). Note that in the interior of the domain we have ${}^2\mathbf{G}_y^u = \mathbf{G}_y^u$ and ${}^2\mathbf{G}_x^v = \mathbf{G}_x^v$. These operators only appear in the lateral mixing of momentum terms (section A.2.5). For the case of $\alpha \neq 2$ (i.e. free-slip, partial-slip or hyper-slip) we might stick to the notation with 2 as prescript but mean the operator defined by equation (A.29), (A.30) for simplicity.

A.2.3 Interpolation

2-point spatial interpolation

With variables that sit on four different grids it is sometimes necessary to transform one variable from one grid onto another. Regarding the term $\partial_x(uh)$ from equation 2.1 we either need to find a representation of u on the T-grid or of h on the u-grid in order to multiply them (the latter is actually preferred, see eq. A.70). This is done via linear interpolation of the closest grid points. In the following we will investigate the interpolations from any of the four grids to any other.

From T-grid to u- or v-grid and vice versa

Let $\mathcal{I}_T^u(\mathtt{h}) = \mathtt{h}_u$ be the linear interpolation of $\mathtt{h}$ from the T-grid (subscript of the interpolation function $\mathcal{I}$) onto the u-grid (superscript of $\mathcal{I}$), then

$$\mathtt{h}_u = h|_{\mathbf{x}=\mathbf{x}_j^u} \approx \frac{h^{\leftarrow} + h^{\rightarrow}}{2} \tag{A.33}$$

which corresponds to spatial averaging of two neighbouring grid points in the x-direction. Similarly to the gradients, we can write this operation via a matrix multiplication with $\mathbf{I}_T^u$ (sub- and superscript meaning as above)

$$\mathcal{I}_T^u : V_T \to V_u, \mathtt{h} \to \mathbf{I}_T^u \mathtt{h} \tag{A.34}$$

Due to the similarity in equation (A.33) and (A.21), $\mathbf{I}_T^u$ is the same as $\mathbf{G}_x^T$ but all non-zero entries replaced by $\frac{1}{2}$. Same holds for the interpolation of $\mathtt{h}$ onto the v-grid, i.e. a spatial averaging in y-direction of two neighbouring grid points

$$\mathtt{h}_v = h|_{\mathbf{x}=\mathbf{x}_k^v} \approx \frac{h^\uparrow + h^\downarrow}{2} \tag{A.35}$$

which can again be written as

$$\mathcal{I}_T^v : V_T \to V_v, \mathtt{h} \to \mathbf{I}_T^v \mathtt{h}. \tag{A.36}$$

with $\mathbf{I}_T^v$ obtained from $\mathbf{G}_y^T$ by setting all non-zero entries to $\frac{1}{2}$. Same relations hold for $\mathbf{I}_q^v$ and $\mathbf{G}_x^q$ (2-point interpolation in x-direction), $\mathbf{I}_q^u$ and $\mathbf{G}_y^q$ (2-point interpolation in y-direction). And also, including the kinematic boundary condition (equation A.1), for $\mathbf{I}_u^T$ and $\mathbf{G}_x^u$ as well as $\mathbf{I}_v^T$ and $\mathbf{G}_y^v$. Interestingly,

$$\mathbf{I}_u^T = \mathbf{I}_T^{u\prime} \quad , \quad \mathbf{I}_v^T = \mathbf{I}_T^{v\prime} \tag{A.37}$$

where $'$ denotes the matrix transpose.

From u-grid and v-grid to q-grid

For the interpolation matrices $\mathbf{I}_u^q, \mathbf{I}_v^q$ the lateral boundary conditions are important. In fact, following the ideas around equation (A.29) we obtain the 2-point interpolation from the u-grid onto the q-grid as

$$\mathtt{u}_q = u|_{\mathbf{x}=\mathbf{x}_l^q} \approx \begin{cases} 0 & \text{if western or eastern boundary} \\ (1-\frac{\alpha}{2})u^\uparrow & \text{if southern boundary without SW,SE} \\ (1-\frac{\alpha}{2})u^\downarrow & \text{if northern boundary without NW,NE} \\ \frac{1}{2}(u^\uparrow + u^\downarrow) & \text{else.} \end{cases} \tag{A.38}$$

with α being the tangential boundary condition parameter ($\alpha = 0$ is free-slip, $\alpha = 2$ is no-slip). Again, $\mathbf{I}_v^q$ is then straight forward

$$\mathtt{v}_q = v|_{\mathbf{x}=\mathbf{x}_l^q} \approx \begin{cases} 0 & \text{if northern or western boundary} \\ (1-\frac{\alpha}{2})v^{\rightarrow} & \text{if western boundary without NW,SW} \\ (1-\frac{\alpha}{2})v^{\leftarrow} & \text{if eastern boundary without NE, SE} \\ \frac{1}{2}(v^{\rightarrow}+v^{\leftarrow}) & \text{else.} \end{cases} \tag{A.39}$$

4-point spatial interpolation

From u-grid to v-grid and vice versa

The previous interpolations involve 2-point spatial averaging, however, the interpolations $\mathcal{I}_u^v, \mathcal{I}_v^u, \mathcal{I}_q^T, \mathcal{I}_T^q$ require averaging from the four surrounding grid points and will be described in the following.

The interpolation $\mathcal{I}_u^v$ from the u-grid onto the v-grid is

$$\mathtt{u}_v = u|_{\mathbf{x}=\mathbf{x}_k^v} \approx \frac{1}{4}\begin{cases} (u^{\searrow}+u^{\nearrow}) & \text{if western boundary} \\ (u^{\swarrow}+u^{\nwarrow}) & \text{if eastern boundary} \\ (u^{\searrow}+u^{\nearrow}+u^{\swarrow}+u^{\nwarrow}) & \text{else.} \end{cases} \tag{A.40}$$

and similarly the interpolation $\mathcal{I}_v^u$ reads

$$\mathtt{v}_u = v|_{\mathbf{x}=\mathbf{x}_j^u} \approx \frac{1}{4}\begin{cases} (v^{\searrow}+v^{\swarrow}) & \text{if northern boundary} \\ (v^{\nearrow}+v^{\nwarrow}) & \text{if southern boundary} \\ (v^{\searrow}+v^{\nearrow}+v^{\swarrow}+v^{\nwarrow}) & \text{else.} \end{cases} \tag{A.41}$$

Note, that both $\mathcal{I}_u^v$ and also $\mathcal{I}_v^u$ include the kinematic boundary condition. Once we write this interpolation as a matrix $\mathbf{I}_u^v$, following the same arguments, we can deduce that

$$\mathbf{I}_v^u = \mathbf{I}_u^{v\prime} \tag{A.42}$$

The interpolation from the u-grid to the v-grid is the transpose of the interpolation from v to u.

From q-grid to T-grid and vice versa

The interpolation $\mathcal{I}_q^T$ from the q-grid to the T-grid is

$$\mathtt{q}_T = q|_{\mathbf{x}=\mathbf{x}_i} \approx \frac{1}{4}(q^{\searrow} + q^{\nearrow} + q^{\swarrow} + q^{\nwarrow}) \tag{A.43}$$

And finally the interpolation $\mathcal{I}_T^q$ makes use of the additional boundary condition in equation A.2 for numerical purposes.

$$\mathtt{h}_q = h|_{\mathbf{x}=\mathbf{x}_l^q} \approx \begin{cases} h^{\swarrow} & \text{if north-east corner (NE)} \\ h^{\searrow} & \text{if north-west corner (NW)} \\ h^{\nwarrow} & \text{if south-east corner (SE)} \\ h^{\nearrow} & \text{if south-west corner (SW)} \\ \frac{1}{2}(h^{\searrow} + h^{\swarrow}) & \text{if northern boundary without NW,NE} \\ \frac{1}{2}(h^{\swarrow} + h^{\nwarrow}) & \text{if eastern boundary without NE,SE} \\ \frac{1}{2}(h^{\nearrow} + h^{\searrow}) & \text{if western boundary without NW, SW} \\ \frac{1}{2}(h^{\nearrow} + h^{\nwarrow}) & \text{if southern boundary without SW, SE} \\ \frac{1}{4}(h^{\searrow} + h^{\nearrow} + h^{\swarrow} + h^{\nwarrow}) & \text{else.} \end{cases} \tag{A.44}$$

A.2.4 Advection term

In the following two different schemes are discussed that aim at discretizing the advection terms

$$(qhv, -qhu), \quad \text{with } q = \frac{f + \partial_x v - \partial_y u}{h} \tag{A.45}$$

with the potential vorticity q, that appear in equation (A.7). The Arakawa and Lamb scheme [Arakawa & Lamb, 1981] used in all model simulations of this study and its implementation is presented in the following.

Arakawa and Lamb (1981) energy and enstrophy conserving scheme

The energy and enstrophy conserving scheme developed by Arakawa & Lamb [1981], called AL hereafter, has a wider stencil compared to the scheme from Sadourny [1975] (hereafter SZ), i.e. computationally more costly, but was

also found to perform better [Salmon, 2007]. That means AL transports less enstrophy (which is essentially squared vorticity) to higher wavenumbers, which reduces the numerical noise on the grid scale compared to SZ. For further details see also Salmon [2004] where the scheme is provided in a much more readable notation as in the original AL paper.

As in SZ compute the mass fluxes $U = uh$ and $V = vh$ as

$$\mathtt{U} = uh|_{\mathbf{x}=\mathbf{x}_j^u} \approx \mathtt{u} * \mathbf{I}_T^u \mathtt{h} \tag{A.46a}$$

$$\mathtt{V} = vh|_{\mathbf{x}=\mathbf{x}_k^v} \approx \mathtt{v} * \mathbf{I}_T^v \mathtt{h} \tag{A.46b}$$

The advective term in the u-component qhv is then discretized as a summation of linear combinations of the surrounding potential vorticity points q and the mass fluxes U, V. We start with computing the linear combinations of q. Let $\mathbf{A}_{L1}, \mathbf{A}_{L2}, \mathbf{A}_{L3}, \mathbf{A}_{L4}$ (without meaning of the subscripts) be four different interpolations[1] (directly written as matrix) fom the q- to the T-grid defined as

$$\mathbf{A}_{L1}\mathtt{q} = \tfrac{1}{24}(2q^{\nwarrow} + q^{\nearrow} + q^{\swarrow} + 2q^{\searrow}), \quad \mathbf{A}_{L2}\mathtt{q} = \tfrac{1}{24}(q^{\nwarrow} + 2q^{\nearrow} + 2q^{\swarrow} + q^{\searrow}) \tag{A.47a}$$

$$\mathbf{A}_{L3}\mathtt{q} = \tfrac{1}{24}(q^{\nwarrow} + q^{\nearrow} - q^{\swarrow} - q^{\searrow}), \quad \mathbf{A}_{L4}\mathtt{q} = \tfrac{1}{24}(q^{\nwarrow} - q^{\nearrow} + q^{\swarrow} - q^{\searrow}) \tag{A.47b}$$

for visualization the corresponding stencils (denoted with subscript $1, 2, 3, 4$) are

$$\tfrac{1}{24}\begin{vmatrix} 2 & 1 \\ 1 & 2 \end{vmatrix}_1, \quad \tfrac{1}{24}\begin{vmatrix} 1 & 2 \\ 2 & 1 \end{vmatrix}_2, \quad \tfrac{1}{24}\begin{vmatrix} 1 & 1 \\ -1 & -1 \end{vmatrix}_3, \quad \tfrac{1}{24}\begin{vmatrix} 1 & -1 \\ 1 & -1 \end{vmatrix}_4 \tag{A.48}$$

We might use $\mathbf{A}_L$ and mean then any of matrices in equation (A.47). We define interpolation matrices $\mathbf{R}$ to get the variables $\mathbf{A}_L\mathtt{q}$ from the T- to the u- or v-grid. As the matrices $\mathbf{R}$ contain a maximum of one entry per row, they are rather shift matrices or correspond to nearest-point interpolation. Hence, they could also be written in terms of an index (as actually done in the model code). We first look at $\mathbf{R}_v^{\uparrow}$ which picks for all v-grid points the

[1] $\mathbf{A}_{L3}$ and $\mathbf{A}_{L4}$ should be rather regarded as potential vorticity gradient due to the minus sign in their stencil.

corresponding $\mathbf{A}_L\mathtt{q}$-value that sits $\frac{1}{2\Delta y}$ North of this point on the T-grid.

$$\mathbf{R}_v^{\uparrow}\mathbf{A}_L\mathtt{q} = (\mathbf{A}_L\mathtt{q})^{\uparrow} \tag{A.49}$$

Hence, the interpolation of this operator shifts the T-grid southward by $\frac{1}{2\Delta y}$ to place them on the v-grid. The grid cell row closest to $y = 0$ is therefore left-out. Similar for $\mathbf{R}_v^{\downarrow}$, $\mathbf{R}_u^{\leftarrow}$ and $\mathbf{R}_u^{\rightarrow}$, which are

$$\mathbf{R}_v^{\downarrow}\mathbf{A}_L\mathtt{q} = (\mathbf{A}_L\mathtt{q})^{\downarrow}, \quad \mathbf{R}_u^{\leftarrow}\mathbf{A}_L\mathtt{q} = (\mathbf{A}_L\mathtt{q})^{\leftarrow}, \quad \mathbf{R}_u^{\rightarrow}\mathbf{A}_L\mathtt{q} = (\mathbf{A}_L\mathtt{q})^{\rightarrow}. \tag{A.50}$$

Once the $\mathbf{A}_L$-interpolated potential vorticity sits on the u- and v-grid they are multiplied with the mass fluxes U, V. In order to get a discretized advection term, AL interpolate the surrounding absolute vorticity fluxes qU, qV onto each u- and v-grid point. For this final interpolation we further need another set of shift-matrices $\mathbf{T}$ (they could again be written in terms of an index) that shift a variable $\mathtt{v}$ from the v to the u-grid as follows

$$\mathbf{T}^{\nearrow}_{v\to u}\mathtt{v} = \begin{cases} 0 & \text{if northern boundary} \\ v^{\nearrow} & \text{else.} \end{cases} \tag{A.51}$$

and include the kinematic boundary condition (case 1). Similarly, we have

$$\mathbf{T}^{\searrow}_{v\to u}\mathtt{v} = \begin{cases} 0 & \text{if southern boundary} \\ v^{\searrow} & \text{else.} \end{cases} \tag{A.52}$$

$$\mathbf{T}^{\swarrow}_{v\to u}\mathtt{v} = \begin{cases} 0 & \text{if southern boundary} \\ v^{\swarrow} & \text{else.} \end{cases} \tag{A.53}$$

$$\mathbf{T}^{\nwarrow}_{v\to u}\mathtt{v} = \begin{cases} 0 & \text{if northern boundary} \\ v^{\nwarrow} & \text{else.} \end{cases} \tag{A.54}$$

and also $\mathbf{T}^{\nwarrow}_{u\to v}, \mathbf{T}^{\nearrow}_{u\to v}, \mathbf{T}^{\searrow}_{u\to v}, \mathbf{T}^{\swarrow}_{u\to v}$ as well as $\mathbf{T}^{\Rightarrow}_{u}, \mathbf{T}^{\Leftarrow}_{u}, \mathbf{T}^{\Uparrow}_{v}, \mathbf{T}^{\Downarrow}_{v}$. We are now

able to write the u-component of the advection term as

$$\begin{aligned} qhv|_{\mathbf{x}=\mathbf{x}_j^u} \approx\ & \mathbf{T}^{\nearrow}_{v\to u}\left(\mathbf{R}_v^{\downarrow}\mathbf{A}_{L1}\mathtt{q} * \mathtt{V}\right) + \mathbf{T}^{\searrow}_{v\to u}\left(\mathbf{R}_v^{\uparrow}\mathbf{A}_{L2}\mathtt{q} * \mathtt{V}\right) \\ & \mathbf{T}^{\nwarrow}_{v\to u}\left(\mathbf{R}_v^{\downarrow}\mathbf{A}_{L2}\mathtt{q} * \mathtt{V}\right) + \mathbf{T}^{\swarrow}_{v\to u}\left(\mathbf{R}_v^{\uparrow}\mathbf{A}_{L1}\mathtt{q} * \mathtt{V}\right) \\ & \mathbf{T}_u^{\Leftarrow}\left(\mathbf{R}_u^{\rightarrow}\mathbf{A}_{L3}\mathtt{q} * \mathtt{U}\right) - \mathbf{T}_u^{\Rightarrow}\left(\mathbf{R}_u^{\leftarrow}\mathbf{A}_{L3}\mathtt{q} * \mathtt{U}\right) \equiv \mathtt{A}_u \end{aligned} \tag{A.55}$$

and the v-component as

$$\begin{aligned} -qhu|_{\mathbf{x}=\mathbf{x}_k^v} \approx\ & -\mathbf{T}^{\nearrow}_{u\to v}\left(\mathbf{R}_v^{\rightarrow}\mathbf{A}_{L1}\mathtt{q} * \mathtt{U}\right) - \mathbf{T}^{\searrow}_{u\to v}\left(\mathbf{R}_v^{\rightarrow}\mathbf{A}_{L2}\mathtt{q} * \mathtt{U}\right) \\ & -\mathbf{T}^{\nwarrow}_{u\to v}\left(\mathbf{R}_v^{\leftarrow}\mathbf{A}_{L2}\mathtt{q} * \mathtt{U}\right) - \mathbf{T}^{\swarrow}_{u\to v}\left(\mathbf{R}_v^{\leftarrow}\mathbf{A}_{L1}\mathtt{q} * \mathtt{U}\right) \\ & -\mathbf{T}_v^{\Uparrow}\left(\mathbf{R}_v^{\downarrow}\mathbf{A}_{L4}\mathtt{q} * \mathtt{V}\right) + \mathbf{T}_v^{\Downarrow}\left(\mathbf{R}_v^{\uparrow}\mathbf{A}_{L4}\mathtt{q} * \mathtt{V}\right) \equiv \mathtt{A}_v \end{aligned} \tag{A.56}$$

These equations correspond to equation B.2 from Salmon [2004] and 3.5 and 3.6 together with 3.34 from Arakawa & Lamb [1981]. However, from this notation it is clear that there are essentially four costly computations that can be precomputed: $\mathbf{A}_{L1}\mathtt{q}, \mathbf{A}_{L2}\mathtt{q}, \mathbf{A}_{L3}\mathtt{q}$ and $\mathbf{A}_{L4}\mathtt{q}$. The remaining shift matrices $\mathbf{R}, \mathbf{T}$ have at maximum one entry per row and can also be implemented as index.

A.2.5 Discrete friction

Discrete bottom friction

We discretize equation (2.6) with the interpolation operators from the previous sections as

$$-\frac{c_D}{h}|\mathbf{u}|u \approx -\frac{c_D}{\mathtt{h}}\mathbf{I}_T^u\left(\sqrt{\mathbf{I}_u^T\mathtt{u}^2 + \mathbf{I}_v^T\mathtt{v}^2}\right) * \mathtt{u} \equiv \mathtt{B}_x \tag{A.57a}$$

$$-\frac{c_D}{h}|\mathbf{u}|v \approx -\frac{c_D}{\mathtt{h}}\mathbf{I}_T^v\left(\sqrt{\mathbf{I}_u^T\mathtt{u}^2 + \mathbf{I}_v^T\mathtt{v}^2}\right) * \mathtt{v} \equiv \mathtt{B}_y \tag{A.57b}$$

In fact, the brackets only have to be computed once, and the term in the square-root also appears in the discrete form of equation (A.5).

Discrete lateral mixing of momentum

The discretization of equation (2.11) is done in the following way:

The stress tensor $\mathbf{S}$ is discretized as

$$\mathbf{S} \approx \begin{pmatrix} \mathbf{G}_x^u \mathtt{u} - \mathbf{G}_y^v \mathtt{v} & {}^2\mathbf{G}_x^v \mathtt{v} + {}^2\mathbf{G}_y^u \mathtt{u} \\ {}^2\mathbf{G}_x^v \mathtt{v} + {}^2\mathbf{G}_y^u \mathtt{u} & -(\mathbf{G}_x^u \mathtt{u} - \mathbf{G}_y^v \mathtt{v}) \end{pmatrix} \equiv \begin{pmatrix} \mathtt{S}_{11} & \mathtt{S}_{12} \\ \mathtt{S}_{12} & -\mathtt{S}_{11} \end{pmatrix} \tag{A.58}$$

Note, as $\mathbf{S}$ is symmetric and has a vanishing trace, only two entries need to be computed explicitly. Then, with $\mathtt{h}_q = \mathbf{I}_T^q \mathtt{h}$

$$\frac{1}{h}\nabla \cdot h\mathbf{S} \approx \begin{pmatrix} \frac{1}{\mathtt{h}_u} * (\mathbf{G}_x^T(\mathtt{h} * \mathtt{S}_{11}) + \mathbf{G}_y^q(\mathtt{h}_q * \mathtt{S}_{12})) \\ \frac{1}{\mathtt{h}_v} * (\mathbf{G}_x^q(\mathtt{h}_q * \mathtt{S}_{12}) - \mathbf{G}_y^T(\mathtt{h} * \mathtt{S}_{11})) \end{pmatrix} \equiv \begin{pmatrix} \mathtt{d}_u \\ \mathtt{d}_v \end{pmatrix} \tag{A.59}$$

which is the harmonic viscosity term without coefficient (which is still assumed to be constant). To obtain a biharmonic viscosity term, we formulate another tensor $\mathtt{R} = (\mathtt{R}_{11}, \mathtt{R}_{12}; \mathtt{R}_{12}, \mathtt{R}_{22})$ as

$$\mathtt{R}_{11} = \mathbf{G}_x^u \mathtt{d}_u - \mathbf{G}_y^v \mathtt{d}_v \tag{A.60a}$$

$$\mathtt{R}_{12} = {}^2\mathbf{G}_x^v \mathtt{d}_v + {}^2\mathbf{G}_y^u \mathtt{d}_u \tag{A.60b}$$

Which is, in principal, evaluating equation (A.58) with $(\mathtt{d}_u, \mathtt{d}_v)$ instead of $(\mathtt{u}, \mathtt{v})$. The divergence of this tensor yields the complete biharmonic lateral mixing of momentum terms

$$\nu_B h^{-1}\nabla \cdot (h\mathbf{S}(h^{-1}\nabla \cdot h\mathbf{S}(u, v))) \approx \nu_B \begin{pmatrix} \frac{1}{\mathtt{h}_u} * (\mathbf{G}_x^T(\mathtt{h} * \mathtt{R}_{11}) + \mathbf{G}_y^q(\mathtt{h}_q * \mathtt{R}_{12})) \\ \frac{1}{\mathtt{h}_v} * (\mathbf{G}_x^q(\mathtt{h}_q * \mathtt{R}_{12}) - \mathbf{G}_y^T(\mathtt{h} * \mathtt{R}_{11})) \end{pmatrix} \equiv \begin{pmatrix} \mathtt{M}_x \\ \mathtt{M}_y \end{pmatrix} \tag{A.61}$$

for a constant biharmonic viscosity coefficient ν_B.

A.2.6 Choosing the viscosity and friction coefficients

The bottom fricton coefficient c_D (equation 2.6) and the biharmonic viscosity ν_B (equation 2.11) that are used in the shallow water model of this study, cannot be chosen from physical principles but their choices should involve considerations of numerical stability [Griffies & Hallberg, 2000]. Arguments for the choice of c_D, ν_B are presented in the following.

Harmonic and biharmonic viscosity

For the given configuration as described in section 2.1.1 we find the choice for the harmonic viscosity

$$\nu_{A,0} = 540\,\mathrm{m}^2\,\mathrm{s}^{-1} \tag{A.62}$$

for a resolution with $\Delta x_0 = \Delta y_0 = 30$ km appropriate once a diffusion operator of the form in equation 2.10 is used. That means it is chosen as small as possible but still removing clearly numerical oscillations that occur at the grid scale. This choice also resolves the Munk boundary layer width [Gill, 1982]

$$W_M = \sqrt[3]{\frac{\nu_{A,0}}{\beta}} \approx \Delta x_0 \tag{A.63}$$

with approximately one grid cell. It was proposed to use this as an argument to set $\nu_A = \beta \Delta x^3$ [Cooper & Zanna, 2015]. Although this might a criterion for stability, for $\Delta x < 30$ km it was not found to prevent numerical oscillations at the grid scale from occuring. Instead, the following scaling argument is proposed: At the grid scale Δx the advective terms are desired to balance with viscosity

$$\mathcal{O}((\mathbf{u}\cdot\nabla)\mathbf{u}) = \frac{U^2}{\Delta x} \sim \nu_A \frac{U}{\Delta x^2} = \mathcal{O}(\nu_A \nabla^2 \mathbf{u}) \tag{A.64}$$

with a velocity scale U. It follows a linear scaling of ν_A with Δx

$$\nu_A = U \Delta x \tag{A.65}$$

under the assumption that the velocity scale does not change considerably with Δx. Based on the empirically found value $\nu_{A,0}$ from equation A.62, it is therefore proposed to use dependent on the resolution

$$\nu_A = \frac{\nu_{A,0}}{\Delta x_0}\Delta x = \frac{540\,\mathrm{m}^2\,\mathrm{s}^{-1}}{30\,\mathrm{km}}\Delta x \tag{A.66}$$

The biharmonic eddy viscosity scaling is derived from the requirement that harmonic and biharmonic viscosity should be on the same order of magnitude

$$1 = \frac{\mathcal{O}(\nu_A \nabla^2 \mathbf{u})}{\mathcal{O}(\nu_B \nabla^4 \mathbf{u})} = \frac{\nu_A}{\nu_B}\Delta x^2 \tag{A.67}$$

Hence, we propose a scaling for ν_B as

$$\nu_B = \frac{\nu_{A,0}}{\Delta x_0}\Delta x^3 = \frac{540\,\mathrm{m^2\,s^{-1}}}{30\,\mathrm{km}}\Delta x^3. \tag{A.68}$$

Based on this equation, we set the biharmonic viscosity coefficients for all model runs as listed in Table 2.1.

Bottom friction coefficient

Arbic & Scott [2008] propose for general purpose a choice of $c_D = 0.0025$ in equation 2.6 based on a comparison of model simulations with observational data. However, using this value in combination with the physical parameters of section 2.1.1 the model reaches a steady state (all $\partial_t \to 0$) within a month or so. Although this steady state resembles a double gyre, no eddies are permitted to develop. Therefore a smaller c_D is needed to reduce the friction in the model. Some tuning experiments lead to the choice of

$$c_D = 10^{-5} \tag{A.69}$$

which removes energy especially on larger scales but retains vorticity dynamics as discussed in the results of chapter 3. The factor 250 discrepancy between our choice and the one from Arbic & Scott [2008] might be further justified as for a one-layer shallow water model the bottom friction is computed via the vertically averaged velocity, not the bottom velocity which would be smaller.

A.2.7 Summary on spatial discretization

The spatially discretized equations of the reformulated shallow water model (equation A.7) are

$$\partial_t u = \mathtt{A}_u - \mathbf{G}_x^T\mathtt{p} + \mathtt{F}_x + \mathtt{B}_x - \mathtt{M}_x \tag{A.70a}$$

$$\partial_t v = \mathtt{A}_v - \mathbf{G}_y^T\mathtt{p} + \mathtt{B}_y - \mathtt{M}_y \tag{A.70b}$$

$$\partial_t \eta = -\mathbf{G}_x^u(\mathtt{u} * \mathbf{I}_T^u\mathtt{h}) - \mathbf{G}_y^v(\mathtt{v} * \mathbf{I}_T^v\mathtt{h}) \tag{A.70c}$$

with

$$\mathtt{p} = \frac{1}{2}\left(\mathbf{I}_u^T(\mathtt{u}^2) + \mathbf{I}_v^T(\mathtt{v}^2)\right) + g\mathtt{h} \tag{A.71}$$

and $\mathtt{A}_u, \mathtt{A}_v$ from equations (A.55,A.56), and $\mathtt{B}_x, \mathtt{B}_y$ from equation (A.57) as well as $\mathtt{M}_x, \mathtt{M}_y$ from equation (A.61).

A.2.8 Time discretization: Runge-Kutta 4th order

The discrete shallow water model is integrated forward in time with the 4th order Runge-Kutta scheme (RK4, Butcher [2008]). Summarizing the right-hand side of equations A.70 with $\mathrm{rhs}(\mathtt{u}, \mathtt{v}, \mathtt{h}) = (\mathtt{du}, \mathtt{dv}, \mathtt{dh})$ the model equations reduce to

$$\partial_t \begin{pmatrix} \mathtt{u} \\ \mathtt{v} \\ \mathtt{h} \end{pmatrix} = \begin{pmatrix} \mathtt{du} \\ \mathtt{dv} \\ \mathtt{dh} \end{pmatrix}. \tag{A.72}$$

Using RK4, discretizing the temporal derivative reads

$$\begin{pmatrix} \mathtt{u}^{n+1} \\ \mathtt{v}^{n+1} \\ \mathtt{h}^{n+1} \end{pmatrix} = \begin{pmatrix} \mathtt{u}^{n} \\ \mathtt{v}^{n} \\ \mathtt{h}^{n} \end{pmatrix} + \frac{\Delta t}{6} \begin{pmatrix} \mathtt{k}_1^u + 2\mathtt{k}_2^u + 2\mathtt{k}_3^u + \mathtt{k}_4^u \\ \mathtt{k}_1^v + 2\mathtt{k}_2^v + 2\mathtt{k}_3^v + \mathtt{k}_4^v \\ \mathtt{k}_1^h + 2\mathtt{k}_2^h + 2\mathtt{k}_3^h + \mathtt{k}_4^h \end{pmatrix} \tag{A.73}$$

with the superscript $n, n+1$ denoting the current and next time step, respectively, that lie time Δt apart. The choice of Δt is discussed in section section A.2.9. $(\mathtt{k}^u, \mathtt{k}^v, \mathtt{k}^h)$ are approximations for $(\partial_t \mathtt{u}, \partial_t \mathtt{v}, \partial_t \mathtt{k})$ and defined as

$$(\mathtt{k}_1^u, \mathtt{k}_1^v, \mathtt{k}_1^h) = \mathrm{rhs}(\mathtt{u}^n, \mathtt{v}^n, \mathtt{h}^n) \tag{A.74a}$$
$$(\mathtt{k}_2^u, \mathtt{k}_2^v, \mathtt{k}_2^h) = \mathrm{rhs}(\mathtt{u}^n + \tfrac{\Delta t}{2}\mathtt{k}_1^u, \mathtt{v}^n + \tfrac{\Delta t}{2}\mathtt{k}_1^v, \mathtt{h}^n + \tfrac{\Delta t}{2}\mathtt{k}_1^h) \tag{A.74b}$$
$$(\mathtt{k}_3^u, \mathtt{k}_3^v, \mathtt{k}_3^h) = \mathrm{rhs}(\mathtt{u}^n + \tfrac{\Delta t}{2}\mathtt{k}_2^u, \mathtt{v}^n + \tfrac{\Delta t}{2}\mathtt{k}_2^v, \mathtt{h}^n + \tfrac{\Delta t}{2}\mathtt{k}_2^h) \tag{A.74c}$$
$$(\mathtt{k}_4^u, \mathtt{k}_4^v, \mathtt{k}_4^h) = \mathrm{rhs}(\mathtt{u}^n + \Delta t\mathtt{k}_3^u, \mathtt{v}^n + \Delta t\mathtt{k}_3^v, \mathtt{h}^n + \Delta t\mathtt{k}_3^h) \tag{A.74d}$$

A.2.9 Choosing the time step Δt

In the shallow water model, the fastest propagating signals are gravity waves. The phase speed c_p of those waves is [Gill, 1982; Vallis, 2006]

$$c_p = \sqrt{gh} \approx \sqrt{gH} \tag{A.75}$$

where the approximation holds in the barotropic case where $|\eta| \ll H$. In contrast, using a reduced gravity $g' \ll g = 10$ m/s^2 usually yields much larger variations in η and the approximation in equation (A.75) may become less justified, but will in many cases still be useful. As a consequence, waves might propagate significantly faster in certain regions, which can affect the numerical stability. The CFL-number ϵ (named after Courant, Friedrichs and Levy; Courant *et al.* [1967]) is then $\epsilon = \frac{c_p \Delta t}{\Delta x}$. Hence, for a desired CFL-number, we obtain the time step Δt as

$$\Delta t = \epsilon \frac{\Delta x}{c_p} \tag{A.76}$$

Using RK4, a choice of $\epsilon \leq 0.9$ was found to be stable in the barotropic set-up of equation 2.2. Multi-step schemes such as Adams-Bashforth [Butcher, 2008] have the advantage, that they only require one evaluation of the right-hand side per time step (in contrast to RK4 which requires 4 evaluations of the right-hand side), which could theoretically decrease the computational time required in order to integrate the model forward. However, in practice, the 3rd order Adams-Bashforth method was found to be stable for $\epsilon \leq 0.2$ (i.e. a decrease of Δt by a factor of 4 to 5), which means that the effective computational performance is on the same order but slightly better with RK4. Therefore all simulations in this study use RK4 with $\epsilon = 0.9$.

A.3 Derivations

A.3.1 Energetics in the shallow water model

The derivation of the energy equation follows the one in Gill [1982] and Vallis [2006] but is here extended to a fully non-linear system. The shallow water equations without forcing or dissipation of momentum and h as the prognostic variable

$$\partial_t u + u\partial_x u + v\partial_y u - fv = -g\partial_x h \tag{A.77a}$$

$$\partial_t v + u\partial_x v + v\partial_y v + fu = -g\partial_y h \tag{A.77b}$$

$$\partial_t h + \partial_x(uh) + \partial_y(vh) = 0 \tag{A.77c}$$

are transformed into an energy equation by (A.77a) $\cdot\, uh$ + (A.77b) $\cdot\, vh$ + (A.77c) $\cdot\, gh$, which results in

$$\underbrace{h\partial_t(\tfrac{1}{2}u^2) + h\partial_t(\tfrac{1}{2}v^2) + \partial_t(\tfrac{1}{2}gh^2)}_{\text{(I)}} + \underbrace{h\mathbf{u}\cdot(\mathbf{u}\cdot\nabla)\mathbf{u}}_{\text{(II)}} + \underbrace{gh\mathbf{u}\cdot\nabla h + gh\nabla\cdot(\mathbf{u}h)}_{\text{(III)}} = 0. \tag{A.78}$$

The terms marked with (I) are with $\kappa = \frac{1}{2}(u^2+v^2)$ and the continuity from equation (A.77c) rearranged to

$$\text{(I)} = \partial_t(h\kappa + \tfrac{1}{2}gh^2) - \kappa\partial_t h = \partial_t(h\kappa + \tfrac{1}{2}gh^2) + \kappa\nabla\cdot(\mathbf{u}h). \tag{A.79}$$

The term marked with (II) is reformulated to

$$\begin{aligned}\text{(II)} &= hu^2\partial_x u + huv\partial_y u + hvu\partial_x v + hv^2\partial_y v \\ &= hu\partial_x(\tfrac{1}{2}u^2) + hv\partial_y(\tfrac{1}{2}u^2) + hu\partial_x(\tfrac{1}{2}v^2) + hv\partial_y(\tfrac{1}{2}v^2) = h\mathbf{u}\cdot\nabla\kappa.\end{aligned} \tag{A.80}$$

Adding (I) and (II) therefore yields

$$\text{(I)} + \text{(II)} = \partial_t(h\kappa + \tfrac{1}{2}gh^2) + \nabla\cdot(\mathbf{u}h\kappa). \tag{A.81}$$

The terms marked with (III) are equal to

$$\text{(III)} = g\nabla\cdot(\mathbf{u}h^2). \tag{A.82}$$

Together, this is

$$\partial_t(h\kappa + \tfrac{1}{2}gh^2) + \nabla\cdot(\mathbf{u}h\kappa + g\mathbf{u}h^2) = 0. \tag{A.83}$$

Horizontal integration $\langle ... \rangle = \int_{\mathcal{D}} ... \,\mathrm{d}\mathbf{x}$ under kinematic boundary conditions eliminiates the divergence term. Multiplying with the constant density ρ for correct unit Joule yields the conservation of energy in the shallow water model

$$\partial_t\langle \rho h\kappa + \tfrac{1}{2}g\rho h^2\rangle = 0 \tag{A.84}$$

which motivates us to call $\rho h\kappa = \frac{1}{2}\rho h(u^2+v^2)$ the (vertically integrated) kinetic energy and $\frac{1}{2}g\rho h^2$ the (vertically integrated) potential energy. As for the initial conditions $u_0 = v_0 = \eta_0 = 0$ the energy in the shallow water system is not zero, we are more interested in the available potential energy

(or perturbation energy) which is obtained by regarding $\eta = h - H$ instead of h. The conservation of mass $\langle \rho h \rangle$ or $\langle \rho \eta \rangle$ is also valid and follows from the continuity equation

$$\partial_t \langle \rho h \rangle = \langle \rho \partial_t h \rangle = \langle -\rho \nabla \cdot (\mathbf{u} h) \rangle = 0 \tag{A.85}$$

which integrates to zero with kinematic boundary conditions. Therefore

$$\partial_t \langle h^2 \rangle = \partial_t \left(\langle \eta^2 \rangle + \langle 2\eta H \rangle + \langle H^2 \rangle \right) = \partial_t \langle \eta^2 \rangle \tag{A.86}$$

and we can replace h by η in equation (A.84) to yield

$$\partial_t \langle \tfrac{1}{2} \rho h (u^2 + v^2) + \tfrac{1}{2} g \rho \eta^2 \rangle = 0. \tag{A.87}$$

A.3.2 Simplifications in the backscatter formulation

We simplify $\nabla \mathbf{u} \cdot \mathbf{S}^*$ with the symmetric, trace-vanishing tensor $\mathbf{S}^* = (\mathbf{S}^*_{11}, \mathbf{S}^*_{12}; \mathbf{S}^*_{12}, -\mathbf{S}^*_{11})$ using the notation $u_x \equiv \partial_x u$

$$\begin{aligned} \nabla \mathbf{u} \cdot \mathbf{S}^* &= u_x \mathbf{S}^*_{11} + v_x \mathbf{S}^*_{12} + u_y \mathbf{S}^*_{12} - v_y \mathbf{S}^*_{11} \\ &= \mathbf{S}_{11} \mathbf{S}^*_{11} + \mathbf{S}_{12} \mathbf{S}^*_{12} \end{aligned} \tag{A.88}$$

so that replacing $\mathbf{S}^*$ by $\mathbf{S}$ yields

$$\nabla \mathbf{u} \cdot \mathbf{S} = \mathbf{S}^2_{11} + \mathbf{S}^2_{12} \tag{A.89}$$

A.3.3 Energetics of the symmetric stress tensor

It is to show that $\nabla \mathbf{u} \cdot \mathbf{S}$ with $\mathbf{S}$ from equation (2.9) is indeed positive definite. It follows in equation (A.89) that

$$\nabla \mathbf{u} \cdot \mathbf{S} = (\partial_x v + \partial_y u)^2 + (\partial_x u - \partial_y v)^2 = |D|^2 \geq 0, \tag{A.90}$$

where $|D|$ is the deformation rate from equation (2.42).

Acknowledgements

I would like to acknowledge

- Richard Greatbatch and Sören Thomsen for right balance of freedom in their supervision as well as the awareness for good science.
- Malte Jansen for incredibly helpful hints and comments on technical details.
- Ole Wulff and Eike Köhn for proofreading and many many helpful discussions, advice and collegial support.
- Martin Claus for the support in the development of the numerical code.
- Fenwick Cooper for many fruitful discussions and the inspiration to do the research you are convinced of. Furthermore, some model runs were performed on his computer.
- everybody involved in the development of Python, NumPy, SciPy, Matplotlib and many other related packages. This study would not have been possible without them.
- and finally my WG for the perfect dinner timing whenever I came home late.

References

Aiki, H., Zhai, X. & Greatbatch, R.J. (2016). Energetics of the Global Ocean : the Role of Mesoscale Eddies. *Indo-Pacific Climate Variability and Predictability*, 109–134. 1, 12

Arakawa, A. & Lamb, V.R. (1977). Computational design of the basic dynamical processes of the UCLA general circulation model. *Methods of Computational Physics*, **17**, 173–265. 59

Arakawa, A. & Lamb, V.R. (1981). A Potential Enstrophy and Energy Conserving Scheme for the Shallow Water Equations. 59, 67, 70

Arbic, B.K. & Scott, R.B. (2008). On Quadratic Bottom Drag, Geostrophic Turbulence, and Oceanic Mesoscale Eddies. *Journal of Physical Oceanography*, **38**, 84–103. 8, 73

Arbic, B.K., Flierl, G.R. & Scott, R.B. (2007). Cascade Inequalities for Forced–Dissipated Geostrophic Turbulence. *Journal of Physical Oceanography*, **37**, 1470–1487. 2

Berloff, P.S. (2005). Random-forcing model of the mesoscale oceanic eddies. *Journal of Fluid Mechanics*, **529**, 71–95. 7

Bigg, G.R., Jickells, T.D., Liss, P.S. & Osborn, T.J. (2003). The role of the oceans in climate. *International Journal of Climatology*, **23**, 1127–1159. 1

Brüggemann, N. & Eden, C. (2015). Routes to Dissipation under Different Dynamical Conditions. *Journal of Physical Oceanography*, **45**, 2149–2168. 15

Butcher, J.C. (2008). *Numerical Methods for Ordinary Differential Equations*. Wiley, 2nd edn. 19, 74, 75

Capet, X., McWilliams, J.C., Molemaker, M.J. & Shchepetkin, A.F. (2008). Mesoscale to Submesoscale Transition in the California Current System. Part III: Energy Balance and Flux. *Journal of Physical Oceanography*, **38**, 29–43. 32

Cooper, F.C. & Zanna, L. (2015). Optimisation of an idealised ocean model, stochastic parameterisation of sub-grid eddies. *Ocean Modelling*, **88**, 38–53. 7, 9, 35, 36, 72

Courant, R., Friedrichs, K. & Lewy, H. (1967). On the Partial Differenc Equations of Mathematical Physics. *IBM Journal of Research and Development*, **11**, 215–234. 75

Eden, C. (2016). Closing the energy cycle in an ocean model. *Ocean Modelling*, **101**, 30–42. 1, 2, 9, 52

Eden, C. & Greatbatch, R.J. (2008). Towards a mesoscale eddy closure. *Ocean Modelling*, **20**, 223–239. ii, iv, 2, 13, 42

Eyring, V., Bony, S., Meehl, G.A., Senior, C.A., Stevens, B., Stouffer, R.J. & Taylor, K.E. (2016). Overview of the Coupled Model Intercomparison Project Phase 6 (CMIP6) experimental design and organization. *Geoscientific Model Development*, **9**, 1937–1958. 1

Ferrari, R. & Wunsch, C. (2009). Ocean Circulation Kinetic Energy: Reservoirs, Sources, and Sinks. *Annual Review of Fluid Mechanics*, **41**, 253–282. 15, 43, 50

Ferrari, R. & Wunsch, C. (2010). The distribution of eddy kinetic and potential energies in the global ocean. *Tellus, Series A: Dynamic Meteorology and Oceanography*, **62**, 92–108. 1

Flato, G., Marotzke, J., Abiodun, B., Braconnot, P., Chou, S., Collins, W., Cox, P., Driouech, F., Emori, S., Eyring, V., Forest, C., Gleckler, P., Guilyardi, E., Jakob, C., Kattsov, V., Reason, C. & Rummukainen, M. (2013). Evaluation of Climate Models. *Climate Change 2013: The Physical Science Basis. Contribution of Working Group I to the Fifth Assessment Report of the Intergovernmental Panel on Climate Change*, 741–866. 1, 26, 51

Gent, P.R. & McWilliams, J.C. (1990). Isopycnal Mixing in Ocean Circulation Models. 2

Gill, A.E. (1982). *Atmosphere-Ocean Dynamics*. Academic Press. 6, 7, 72, 74, 75

Greatbatch, R.J., Zhai, X., Claus, M., Czeschel, L. & Rath, W. (2010). Transport driven by eddy momentum fluxes in the Gulf Stream Extension region. *Geophysical Research Letters*, **37**, 1–6. 2

Griffies, S.M. (2004). Fundamentals of ocean climate models. *Princeton University Press*, 518 pp. 2, 12

Griffies, S.M. & Hallberg, R.W. (2000). Biharmonic Friction with a Smagorinsky-Like Viscosity for Use in Large-Scale Eddy-Permitting Ocean Models. *Monthly Weather Review*, **128**, 2935–2946. 2, 10, 31, 43, 51, 71

Jansen, M.F. & Held, I.M. (2014). Parameterizing subgrid-scale eddy effects using energetically consistent backscatter. *Ocean Modelling*, **80**, 36–48. ii, iv, 2, 13, 31, 42, 43, 52

Jansen, M.F., Held, I.M., Adcroft, A. & Hallberg, R. (2015). Energy budget-based backscatter in an eddy permitting primitive equation model. *Ocean Modelling*, **94**, 15–26. ii, iv, 2, 13, 14, 15, 18, 31, 42, 43, 45, 46, 48, 50, 51, 52

Large, W.G. & Danabasoglu, G. (2006). Attribution and impacts of upper-ocean biases in CCSM3. *Journal of Climate*, **19**, 2325–2346. 26

Leith, C.E. (1967). Diffusion Approximation to Inertial Energy Transfer in Isotropic Turbulence. *Physics of Fluids*, **10**, 1409. 51

Madec, G. (2016). NEMO ocean engine. *Note du Pole de modelisation de l'Institut Pierre-Simon Laplace*, **27**. 63

Marshall, J.C. (1984). Eddy-mean flow interaction in a barotropic ocean model. 1, 23

McWilliams, J.C. (2016). Submesoscale currents in the ocean. *Proceedings of the Royal Society of London A*, **472**, 1–32. 1

Molemaker, M.J., McWilliams, J.C. & Yavneh, I. (2005). Baroclinic Instability and Loss of Balance. *Journal of Physical Oceanography*, **35**, 1505–1517. 43

Molemaker, M.J., McWilliams, J.C. & Capet, X. (2010). Balanced and unbalanced routes to dissipation in an equilibrated Eady flow. *Journal of Fluid Mechanics*, **654**, 35–63. 15, 43, 50

Palmer, T.N. (2001). A nonlinear dynamical perspective on model error: A proposal for non-local stochastic-dynamic parametrization in weather and climate prediction models. *Quarterly Journal of the Royal Meteorological Society*, **127**, 279–304. 2

Palmer, T.N. (2012). Towards the probabilistic Earth-system simulator: A vision for the future of climate and weather prediction. *Quarterly Journal of the Royal Meteorological Society*, **138**, 841–861. 22, 28

Porta Mana, P.G.L. & Zanna, L. (2014). Toward a stochastic parameterization of ocean mesoscale eddies. *Ocean Modelling*, **79**, 1–20. 2, 7

Randall, D., Wood, R., Bony, S., Colman, R., Fichefet, T., Fyfe, J., Kattsov, V., Pitman, A., Shukla, J., Srinivasan, J., Stouffer, R., Sumi, A. & Taylor, K. (2007). Climate models and their evaluation. *Climate Change 2007: The Phisical Science Basis. Contribution of Working Group I to the Fourth Assessment Report on the Intergovernmental Panel on Climate Change*. 1

Rhines, P.B. (1979). Geostrophic Turbulence. *Annual Review of Fluid Mechanics*, **11**, 401–441. 15, 50

Sadourny, R. (1975). The Dynamics of Finite-Difference Models of the Shallow-Water Equations. 67

Salmon, R. (2004). Poisson-Bracket Approach to the Construction of Energy- and Potential-Enstrophy-Conserving Algorithms for the Shallow-Water Equations. *Journal of the Atmospheric Sciences*, **61**, 2016–2036. 68, 70

Salmon, R. (2007). A General Method for Conserving Energy and Potential Enstrophy in Shallow-Water Models. *Journal of the Atmospheric Sciences*, **64**, 515–531. 68

Scott, R.B. & Wang, F. (2005). Direct Evidence of an Oceanic Inverse Kinetic Energy Cascade from Satellite Altimetry. *Journal of Physical Oceanography*, **35**, 1650–1666. 43

Shchepetkin, A.F. & O'Brien, J.J. (1996). A Physically Consistent Formulation of Lateral Friction in Shallow-Water Equation Ocean Models. 9, 10, 63

Shutts, G. (2015). A stochastic convective backscatter scheme for use in ensemble prediction systems. *Quarterly Journal of the Royal Meteorological Society*, **141**, 2602–2616. 22

Smagorinsky, J. (1963). General Circulation Experiments With the Primitive Equations. *Monthly Weather Review*, **91**, 99–164. 51

Vallis, G.K. (2006). *Atmospheric and Ocean Fluid Dynamics*. Cambridge University Press. 6, 74, 75

Vallis, G.K. (2016). Geophysical fluid dynamics: whence, whither and why? *Proceedings of the Royal Society A: Mathematical, Physical and Engineering Science*, **472**, 20160140. 1

Verdiere, A. (2009). Keeping the freedom to build idealized climate models. *Eos*, **90**, 2009. 51

Wagner, P. (2017). *Eulerian and Lagrangian tracer spreading in an high resolution Ocean General Circulation Model*. Ph.D. thesis, University of Kiel. 38

Wunsch, C. (2002). What Is The Thermohaline Circulation? *Science*, **298**, 1179–1181. 1

Wunsch, C. & Ferrari, R. (2004). Vertical Mixing, Energy, and the General Circulation of the Oceans. *Annual Review of Fluid Mechanics*, **36**, 281–314. 1

Zanna, L., Porta Mana, P., Anstey, J., David, T. & Bolton, T. (2017). Scale-aware deterministic and stochastic parametrizations of eddy-mean flow interaction. *Ocean Modelling*, **111**, 66–80. 2, 7

Zhai, X., Johnson, H.L. & Marshall, D.P. (2010). Significant sink of ocean-eddy energy near western boundaries. *Nature Geoscience*, **3**, 608–612. 15, 44

Statement / Erklärung

I hereby declare that I have written the master's thesis on my own and have used no other than the stated sources and aids. The submitted written version is equivalent to the electronical data medium. Furthermore, I affirm that this work has not been submitted for any other degree.

Hiermit erkläre ich, dass ich die vorliegende Masterarbeit selbstständig und ohne fremde Hilfe angefertigt und keine anderen als die angegebenen Quellen und Hilfsmittel verwendet habe. Die eingereichte schriftliche Fassung der Arbeit entspricht der auf dem elektronischen Speichermedium. Weiterhin versichere ich, dass diese Arbeit noch nicht als Abschlussarbeit an anderer Stelle vorgelegen hat.

Milan Klöwer
Kiel, September 14, 2017